NTNU – Trondheim
Norwegian University of
Science and Technology

Synthesis and Characterization of Hydrogen Transport Membranes

Lasse Valland Roaas

Materials Technology
Submission date: June 2012
Supervisor: Paul Inge Dahl, IMTE

Norwegian University of Science and Technology
Department of Materials Science and Engineering

Declaration

I hereby declare that the work performed in this master thesis has been done independently, and in accordance with the rules and regulations which regulates the master programs at the Norwegian University of Science and Technology, NTNU.

Trondheim, June 27, 2011

_____

Lasse Valland Roaas

Preface

This master thesis has been carried out at The Department of Material Science and Technology at The Norwegian University of Science and Technology during the spring of 2012.

Numerous people have helped me with experimental work, theoretical discussions, editing and encouragement throughout the semester. They all deserve my gratitude and are highly appreciated.

First and foremost, I wish to express my sincere gratitude to my supervisor Ph.D Paul Inge Dahl, senior scientist at SINTEF Materials and Chemistry, for the invaluable guidance, discussions and availability throughout the whole semester.

I would also like to thank Professor Mari-Ann Einarsrud and the soild oxide fuel cell group at NTNU for giving me valuable input on membrane technology and affiliation in the research group. Special thanks to group member and senior engineer Julian R Tolchard for conducting lattice parameter measurements.

Abstract

Hydrogen transport membranes have gained interest from industry as an alternative to pressure swing adsorption or cryogenic distillation, and are aimed to reduce cost, equipment size, energy consumption and waste generation. Doped strontium cerate stabilized with zirconium exhibit high proton conductivity and chemical stability and is therefore considered to be a promising material for hydrogen transport membranes.

The purpose of the work was to investigate if phase pure strontium cerates, stabilized with zirconium and doped with thulium, ytterbium or yttrium, could be synthesized by the Pechini method, and if the membranes exhibited sufficient density. Determination of optimal calcination and sintering parameters was also important parts in the study.

$SrCe_{0.75}Zr_{0.20}M_{0.05}O_{3-\delta}$, (M=Tm,Y,Yb) were synthesized via the Pechini method, followed by calcination, pressing of green bodies and sintering of dense membranes. Phase purity of powders and sintered membranes was examined by X-ray diffraction. Surface investigation and microstructure was investigated in a scanning electron microscope. Sintering behavior and thermal expansion coefficients was determined by dilatometry.

Phase pure and dense orthorhombic perovskite structured $SrCe_{0.75}Zr_{0.20}M_{0.05}O_{3-\delta}$, (M=Tm,Y,Yb) membranes, were obtained by powder calcination at 1000 ˚C, followed by milling and conventional sintering at 1500˚C-1600 ˚C. $SrCe_{0.75}Zr_{0.20}Tm_{0.05}O_{3-\delta}$ demonstrated the highest density of 98,6%, when sintered at 1500 ˚C. Sintered membranes had an average grain size in the range from 3,2 μm-4,9 μm. Ball milling is concluded to be of vital importance to obtain sufficient density in the membranes.

The membrane characterization is limited to the methods and techniques described above. Hydrogen flux across the membrane, total conductivity, stability in reducing atmosphere and thorough investigation of thermal properties are recommended for further work.

Sammendrag

Hydrogen transport membraner har fått en økt interesse fra industrien som et alternativ til kryogenisk destillasjon eller trykk sving adsorpsjon, som et ledd i å minke kostnader, størrelse på utstyr, energi forbruk og avfall. Dopet strontium cerat stabilisert med zirkonium viser høy protonisk ledningsevne og kjemisk stabilitet og er derfor ansett som et lovende materiale for hydrogen transport membraner.

Bakgrunnen for oppgaven var å undersøke om fase rent strontium cerat, stabilisert med zirkonium og dopet med enten thulium, ytterbium eller yttrium kunne bli syntetisert ved bruk av Pechini metoden, og om membranene viste tilstrekkelig tetthet. Kartlegging av optimale sintrings og kalsinerings parametere var også en viktig del av oppgaven.

$SrCe_{0.75}Zr_{0.20}M_{0.05}O_{3-\delta}$, (M=Tm,Y,Yb) ble syntetisert via Pechini metoden, med påfølgende kalsinering, pressing av grønnkropper og sintring av tette membraner. Fase renheten til membranene ble undersøkt med røntgen diffraksjon. Overflate og mikrostruktur ble karakterisert ved bruk av scanning elektron mikroskop. Sintringsforløpet og termisk utvidelseskoeffisient ble bestemt ved hjelp av dilatometri.

Fase rene og tette $SrCe_{0.75}Zr_{0.20}M_{0.05}O_{3-\delta}$, (M=Tm,Y,Yb) membraner med ortorombisk perovskitt struktur ble oppnådd ved kalsinering av pulveret ved 1000 ˚C, mølling og påfølgende sintring ved 1500˚C-1600 ˚C. Det ble oppnådd en tetthet på 98,6% av teoretisk tetthet ved sintring av $SrCe_{0.75}Zr_{0.20}Tm_{0.05}O_{3-\delta}$ ved 1500 ˚C. De sintrede membranene hadde en gjennomsnittlig kornstørrelse mellom 3,2 µm-4,9 µm. Mølling av pulveret viste seg å være kritisk for å oppnå tilstrekkelig tetthet i membranene.

Karakterisering av membranene er begrenset til de metoder og teknikker som er nevnt ovenfor. Hydrogen gjennomstrømning, total ledningsevne, stabilitet i reduserende atmosfære og grundig undersøkelse av termiske egenskaper er anbefalt som videre arbeid

Content

List of Acronyms

SC	$SrCeO_3$
SCZ	$SrCe_{0.75}Zr_{0.25}O_{3-\delta}$
SCZT	$SrCe_{0.75}Zr_{0.20}Tm_{0.05}O_{3-\delta}$
SCZY	$SrCe_{0.75}Zr_{0.20}Y_{0.05}O_{3-\delta}$
SCZYb	$SrCe_{0.75}Zr_{0.20}Yb_{0.05}O_{3-\delta}$
SEM	Scanning Electron Microscope
SZ	$SrZrO_3$
TEC	Thermal Expansion Coefficient
XRD	X-ray diffraction

1. Introduction

There is a global push to develop a range of hydrogen technologies for timely adoption of the hydrogen economy. This is critical in view of the depleting oil reserves, transport fuel shortage, global warming, and increasing pollution. Hydrogen gas can be generated by a number of renewable and fossil-fuel-based resources. Effective technologies are required for the separation of hydrogen from a gas feed, and can be done by pressure swing adsorption, cryogenic distillation or membrane separation [1]. The membranes need to withstand aggressive chemical environments, high temperature and large pressure gradients. Polymer membranes exhibit large hydrogen flux, but have a tendency to swell or plasticize during operation in these conditions and their separation capabilities is reduced [2]. Palladium thin-film membranes are stable at medium temperatures up to 500 ˚C, and exhibit an extraordinary hydrogen flux [3]. If the temperature in the membrane reactor is even higher, mixed conducting membranes, based on ceramic materials, is a promising candidate, due to high stability, mechanical strength and direct reforming on the membrane surface.

In the early 1980s, Iwahara et al. [4] firstly reported proton conductivity in doped $SrCeO_3$ perovskite materials in hydrogen-containing atmosphere at high temperature (>600 ˚C). Later, protonic conductivity was also demonstrated in other doped perovskites [5], and researchers strive to increase both the hydrogen flux across the membrane and the stability in reducing atmospheres by incorporation of different dopants. $SrCeO_3$ is still one of the best proton conducting materials and exhibit high hydrogen flux. When investigating new membrane material compositions, a considerable amount of work has to be done with regard to synthesis and characterization.

The purpose of the work was to investigate if phase pure strontium cerates, stabilized with zirconium and doped with thulium, ytterbium or yttrium, could be synthesized by the Pechini method, and if the membranes exhibited sufficient density. Optimal calcination and sintering parameters were also studied. Phase purity of powders and sintered membranes was examined by X-ray diffraction. Surface investigation and microstructure was investigated in scanning electron microscope. Sintering behavior and thermal expansion coefficients was determined by dilatometry.

2. Theory

2.1 Material properties

2.1.1 Perovskite structure

The general formula for perovskite structures is ABO_3. A is a large cation and B is a medium sized cation. Oxygen is connected to both of them, giving the coordination formula of $A^{XII}B^{VI}O_3$ with valences of $A^{+2}B^{+4}O_3$ ($A^{+3}B^{+3}O_3$ and $A^{+1}B^{+5}O_3$ are also possible) [6]. The ideal cubic perovskite structure is shown in Figure 1. A is situated in the middle of the cube, and B at each corner. Oxygen has an octahedron configuration, and is represented by red spheres.

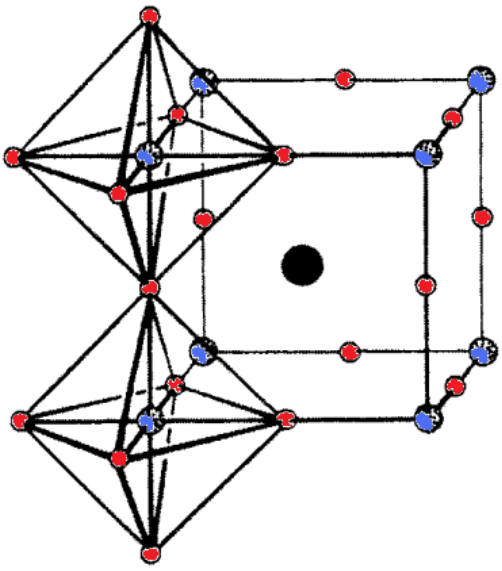

Figure 1 Ideal cubic perovskite structure, modified from [6]. A, B and O sites is represented by black, blue and red spheres, respectively

The perovskite structure is preserved if the tolerance factor t, given in equation 2.1 is between 0,8 and 1,0 as stated by Goldsmith [7]. The tolerance factor or degree of distortion for $SrCeO_3$ is equal to 0.889, giving it an orthorhombic distorted perovskite structure shown in Figure 2 (b). The ideal cubic perovskite structure is represented by t=1.

$$t = \frac{R_A + R_O}{\sqrt{2(R_B + R_O}} \quad (2.1)$$

Where R_A, R_B and R_O is the ionic radii of cation A, B and Oxygen, respectively.

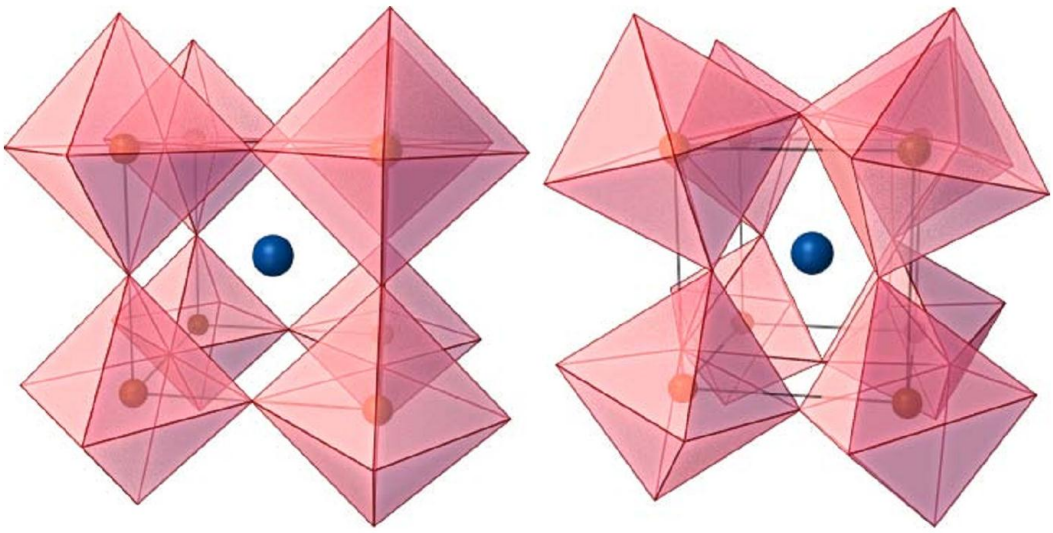

(a) *(b)*

Figure 2 Perovskite distortion from (a) cubic to (b) orthorhombic [8]

All perovskite distortions that maintain the A and B site oxygen coordination, involve the tilting of the BO_6 octahedra and an associated displacement of the A cation. For the orthorhombic structure, these octahedral tilt about the b and c axes [8].

When doping is introduced in to the structure, the lattice parameters changes due to different ionic radii of the dopant, compared to the parent cation. Table 1 presents lattice parameters of some orthorhombic strontium based materials.

Table 1 Lattice parameters in doped and not doped $SrCeO_3$ or $SrZrO_3$ [9-11]

	a [nm]	b [nm]	c [nm]	V [nm^3]	ρ [g/cm^3]
$SrCeO_3$	0.6147	0.8585	0.6006	0.317	5.77
$SrZrO_3$	0.5817	0.8204	0.5799	0.277	5.44
$SrCe_{0.75}Zr_{0.20}Tm_{0.05}O_{3-\delta}$	0.5969	0.8519	0.6074	0.309	5.75
$SrCe_{0.70}Zr_{0.25}Yb_{0.05}O_{3-\delta}$	0.6061	0.8487	0.5951	0.306	5.77

The ionic radii of the dopants and the parenting cerium cation are presented in Table 2.

Table 2 Shannon ionic radii of parent cation and dopands of interest

Cation	**Shannon ionic radii [Å]**
Ce^{4+}	0,87
Zr^{4+}	0,72
Tm^{3+}	0,88
Yb^{3+}	0,868
Y^{3+}	0,9

2.1.2 Transport mechanisms and doping

A simplified overview of hydrogen transport through a dense mixed conducting membrane is shown in Figure 3. The transport of hydrogen is based on the solution-diffusion mechanism. The hydrogen transport is driven by a chemical potential gradient across the membrane, and can be controlled by the pressure gradient, concentration gradient, temperature gradient, or electric field gradient. Typically a hydrostatic gradient is used to promote the transport of H_2 through the membrane [1].

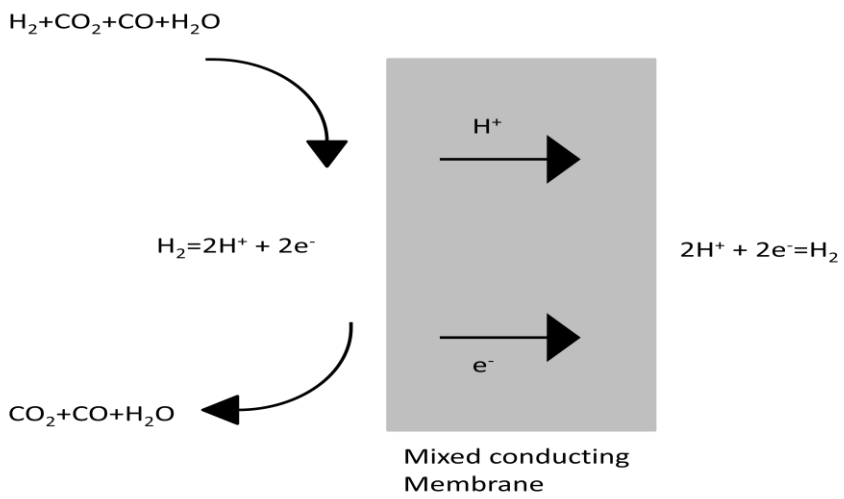

Figure 3 Schematic representation of H_2 transport steps trough mixed conducting membrane, modified from [1]

The simplest route from hydrogen gas to protons dissolved in the oxide is shown in equation 2.2 and 2.3 [12].

$$H_{2(g)} + 2v_{ads} = 2H_{ads} \tag{2.2}$$

$$H_{ads} + O_O^{\times} = OH_O^{\bullet} + e^{-} + v_{ads} \tag{2.3}$$

Where v_{ads} denotes a free active site, H_{ads} is an adsorbed proton, $O_O^{\times}$ is oxygen at regular site, $OH_O^{\bullet}$ is a hydroxide ion and e^- is an electron.

Protons do not migrate through the membrane as free interstitial ions, but is strongly associated with an O^{2-} ion, forming a hydroxide ion. The proton jumps from one O^{2-} to another through the membrane [12].

Doped $SrCeO_3$ exhibit a great potential as hydrogen separation membrane due to its high ionic conductivity, but the chemical stability and electric conductivity is low. As seen in Figure 3, the hydrogen flux across the membrane is dependent on both the transport of electrons and protons. To increase the hydrogen flux, electron conductivity must be enhanced.

The electronic hopping mechanism in semiconductors occurs between two neighboring ions with different valences [13]. In perovskites the BO_6 octahedra is connected to each other, and is responsible for electronic conduction. It is known that substituting the B site cation with dopants with different valence, often rare earth metals, can increase the electronic conductivity. The electronic hopping mechanism between cerium and e.g. thulium can be represented by equation 2.4 and 2.5.

$$Ce^{4+} + h^{\bullet} = Ce^{3+} \tag{2.4}$$

$$Tm^{3+} + h^{\bullet} = Tm^{2+} \tag{2.5}$$

If Ce^{4+} ions are replaced by a tree valiant ion e.g. Tm^{3+} an oxygen vacancy is created to maintain electrical neutrality. The oxygen vacancy tends to react with oxygen gas and create electron holes. This will enhance the electric conductivity. In dry air the following equilibrium is established [14]:

$$VO^{\bullet\bullet} + ½O_2 = O_O^{\times} + 2h^{\bullet} \tag{2.6}$$

Where $VO^{\bullet\bullet}$,$O_O^{\times}$ and $h^{\bullet}$, denotes oxygen vacancy, oxygen at regular site and electron hole, respectively.

Zr^{4+} is stable without charge transfer and has the same valence as Ce^{4+} and will therefore not enhance the electrical conductivity [10]. Strontium zirconates exhibit lower proton conductivity, but has higher mechanical strength and chemical resistance than strontium cerate based ceramics. Strontium cerate show a tendency to react with CO_2, according to equation 2.7 [15, 16].

$$SrCeO_3(s) + CO_2(g) = SrCO_3(s) + CeO_2(s) \tag{2.7}$$

It is a trade off with respect to the stability and conductivity when introducing zirconium to the B-site. An increase of zirconium content in the structure will increase the chemical and mechanical stability, but lower the protonic conductivity resulting in lower hydrogen flux [17]. Liang, J et.al [10] found a significant drop in the total conductivity in SCZT, when increasing the zirconium doping level from 20 to 30 mol%.

Generally, the H_2 permeation flux across a mixed-ionic conducting membrane is described by the Wagner equation given in equation 2.8, which assumes the bulk diffusion as the rate-limiting step:

$$J_{H2} = \frac{RT}{4F^2L} \int_{P'_{H2}}^{P''_{H2}} \frac{\sigma_{OH^{\cdot}}(\sigma_{h^{\cdot}+\sigma_{e'}})}{\sigma_t} dlnP_{H_2} \tag{2.8}$$

Were J_{H2} is the hydrogen flux, L is the thickness of the membrane, F is Faradays constant, R is the gas constant and T is temperature. P´´ and p´ denotes the partial pressure of hydrogen at the feed and permeate side. σ is the conductivity and subscripts $OH^{\cdot}$, $h^{\cdot}$, t and e' denote proton at oxygen site, electron hole, total conductivity and electron, respectively [18].

Studies by Hamakawa et.al [19] confirms that the hydrogen permeation flux is proportional to the inverse membrane thickness. This indicates that surface kinetics does not affect the rate-limiting step of hydrogen permeation.

Since the hydrogen flux is proportional to the inverse membrane thickness, thinner membranes is advantageous. Thin-film membranes do not have sufficient mechanical strength to withstand high pressure, so it must be supported. The support has a continuous pore structure to promote gas permeation [20].

2.2 Synthesis

Strontium cerates have been synthesized by a range of different processes routes such as, the common solid-state-reaction [9], spray pyrolysis [21], combustion synthesis [22] and liquid mix processes [10]. It is widely recognized that the densification behavior is highly dependent on powder characteristics such as particle size, particle size distribution, surface area and morphology [14].

The solid-state-reaction process has been the most common synthesis route when producing ceramic powder. It is well established, but a time consuming and costly process. The powder is often coarse and agglomerated due to high calcination temperatures. The process can also result in a heterogeneous powder if the powder is not evenly distributed when calcined [14].

2.2.1 The Pechini method

Liquid mix process is a process that starts with a homogeneous solution containing the desired cations, which use additives and evaporation to convert the homogeneous liquid to a rigid cross-linked polymer. Heat is applied to convert the polymer into a homogeneous oxide powder. This process was pioneered by Maggio Pechini [23] in 1967 and is referred to as the Pechini method or the amorphous citrate process. The process was originally developed to prepare metal oxide powders such as titanates and niobates for capacitors.

The process includes the following steps:

1. An aqueous solution of nitrates, oxides (soluble), carbonates, metal alcoxides or hydrated oxides is prepared. Citric acid is added to create metal citrate complexes.
2. A polyhydoxy alcohol such as ethylene glycol is added and heat is applied to allow chelates to undergo polyesterfication.
3. Heating is continued to remove excess water, resulting in a solid polymeric resin. Further heating results in decomposition of the resin as it ignites and most of the hydrocarbons are burned off.
4. Calcination to burn off remaining hydrocarbons and form crystallites of the mixed oxide composition.

Step 1 and 2 is visualized in Figure 4.

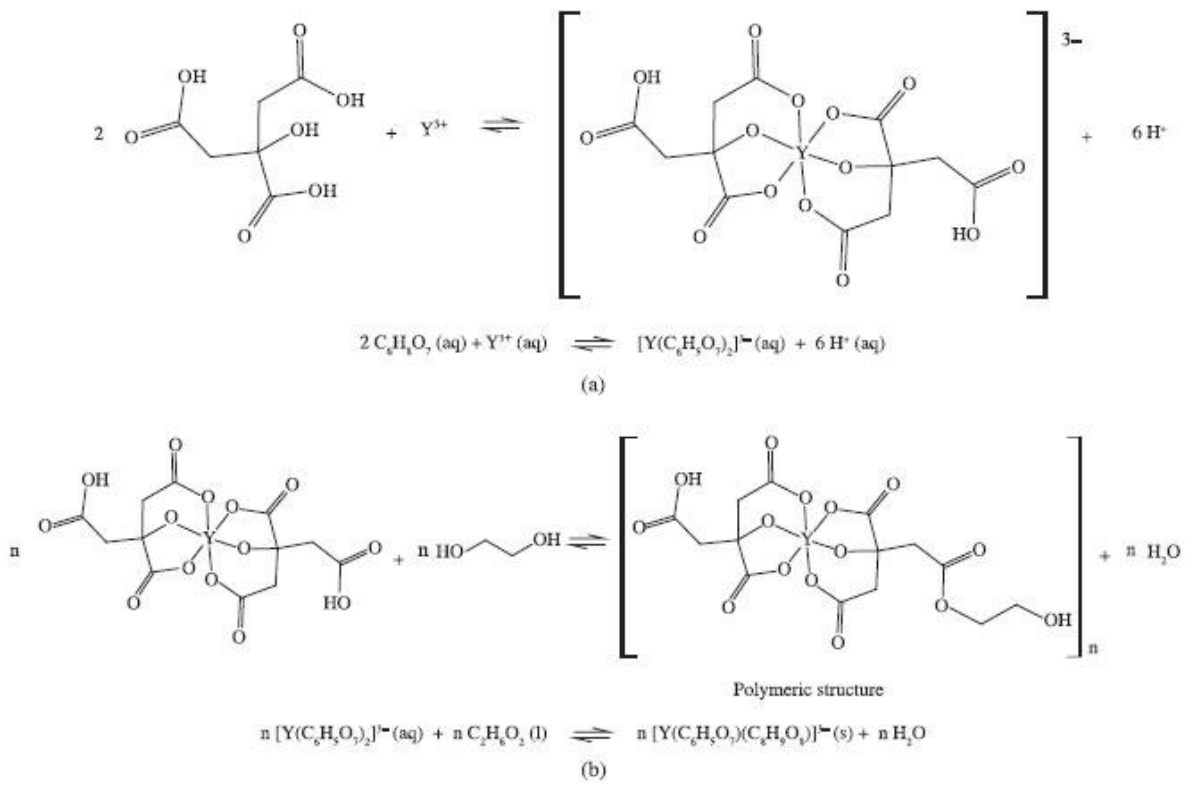

Figure 4 Schematic representation of a) metal-citric acid complex and b) polymeric precursor formation[24]

The main advantage of the Pechini method is that you can achieve a homogeneous powder and relative small particle sizes. The crystallites is typically 20 to 50 nm and clustered into agglomerates [25].

2.3 Characterization

2.3.1 X-Ray diffraction

X-ray diffraction (XRD) is non-destructive characterization technique that can determine crystal phases, orientation and structural properties. It is an important step in the quality assurance of ceramic materials. It utilizes X-ray beams that irradiate the surface of a specimen and various intensities are registered at different incident angles.

A heated tungsten filament generates an electron beam, which is accelerated towards an anode by a potential difference (30 kV), and hit a piece of copper attached to the anode. The incoming electrons have sufficient energy to ionize a 1s electron, which leads to an empty spot in the 1s orbital. An electron in the 2p or 3p drops down to the lower energy level in 1s, and the energy difference is emitted as an X-ray. Depending on which outer orbital the electron drops from, the wavelength of the X-ray varies. A drop from 2p is known as K_α radiation, and a drop from 3p is K_β radiation. To absorb the unwanted wavelengths, a filter is applied, so that only K_α radiation is emitted [26].

When the X-ray hits a sample, scattering is produced in all directions. Diffraction redistributes intensity from the scattering sphere into distinct directions and the intensity increases in certain directions [27]. Constructive interference only occurs when Bragg's law is satisfied, and is given in equation 2.9.

$$n\lambda = 2d\sin\theta \tag{2.9}$$

Were n is an integer, λ is the wavelength, d is the atomic spacing and θ is the angle between lattice planes and the X-ray beam

A geometric derivation of Bragg's law is presented in Figure 5. Constructive interference occurs when the delay between waves scattered from adjacent lattice planes given by $a_1 + a_2$ is an integer multiple of the wavelength λ.

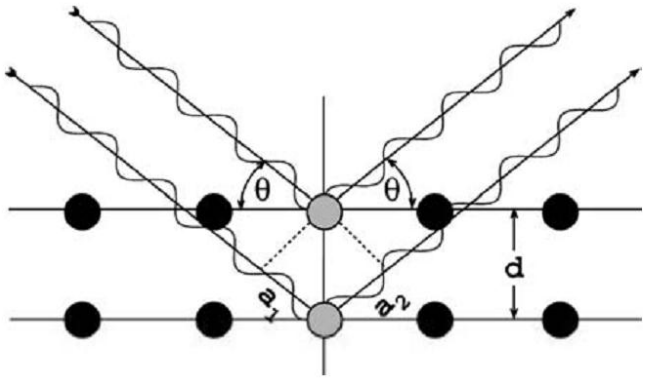

Figure 5 Geometric derivation of Bragg's law [27].

By changing the angle of incident X-ray beam e.g. from 10 to 80 degrees, intensity peaks arise at certain angles depending on the unit cell geometry. Each crystalline powder has its own characteristic X-ray powder pattern which can be used for identification. By searching and comparing patterns from a data base, the phase and composition of an unknown powder can be determined fast and accurately. The significance of each phase can be determined by the peak intensity, width and position in the XRD pattern.

2.3.2 Scanning electron microscope

The scanning electron microscope (SEM) permits observation and characterization of organic or inorganic materials on nano or micrometer scale. It is a popular technique due to the high resolution and the depth of field obtained in the images. The area to be analyzed is swept by a finely focused electron beam, and the interaction between the electron beam and the sample give rise to different signals picked up by the respective detectors [28].

The electron gun, normally a tungsten filament, emits electrons that are accelerated towards an anode. The potential difference between anode and cathode is in the interval 1-40 kV. The electrons travel through a column subjected to a vacuum. The column consists of tree magnetic lenses that focus the electron beam, an aperture to limit the beam divergence and a scanning coil. When the electron beam hits the sample secondary electrons, backscatter electrons, X-rays, Auger electrons or photons may be detected. Normal SEM images consist of signals from backscatter or secondary electrons [29]. Schematic of a typical SEM is presented in Figure 6.

When a signal is detected, it is amplified and sent to a display unit. Since the scanning of the display unit is synchronized with the electron probe scan, brightness variations depending on the number of electrons detected in that area appears on the monitor screen. These variations in intensity make up the SEM image.

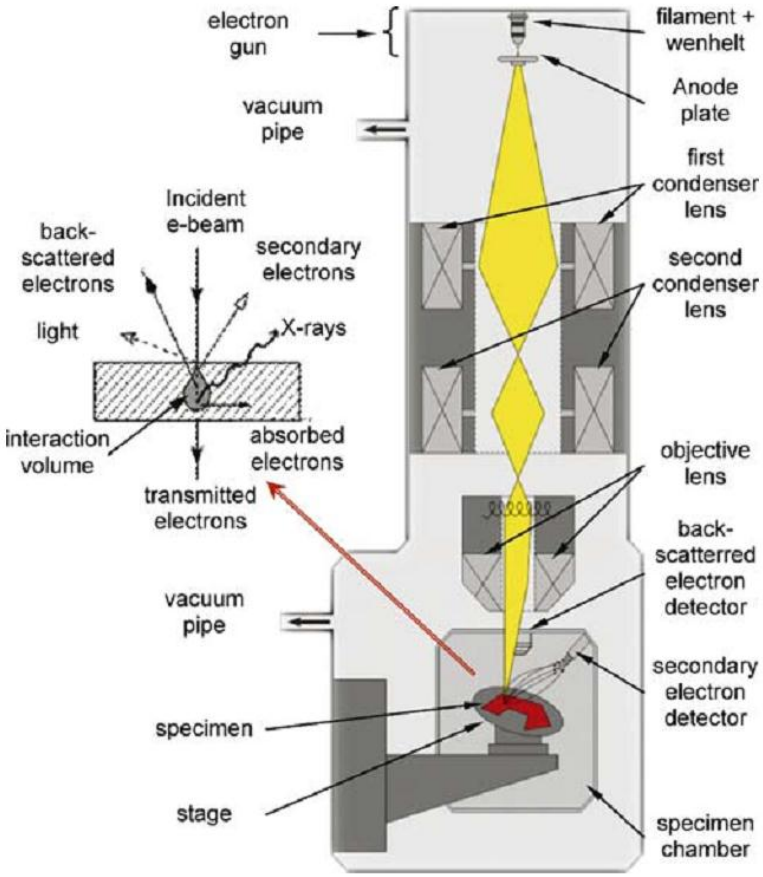

Figure 6 Schematic of a typical SEM [30]

2.3.3 Dilatometry

Dilatometry is a thermo-analytic technique that measures the volume change of powders, solids, liquids or paste during heating or cooling. Accurate understanding of the data obtained, can provide insight about sintering properties, phase transitions, reaction kinetics, the influence of additives and thermal expansion.

A horizontal dilatometer is shown in Figure 7.

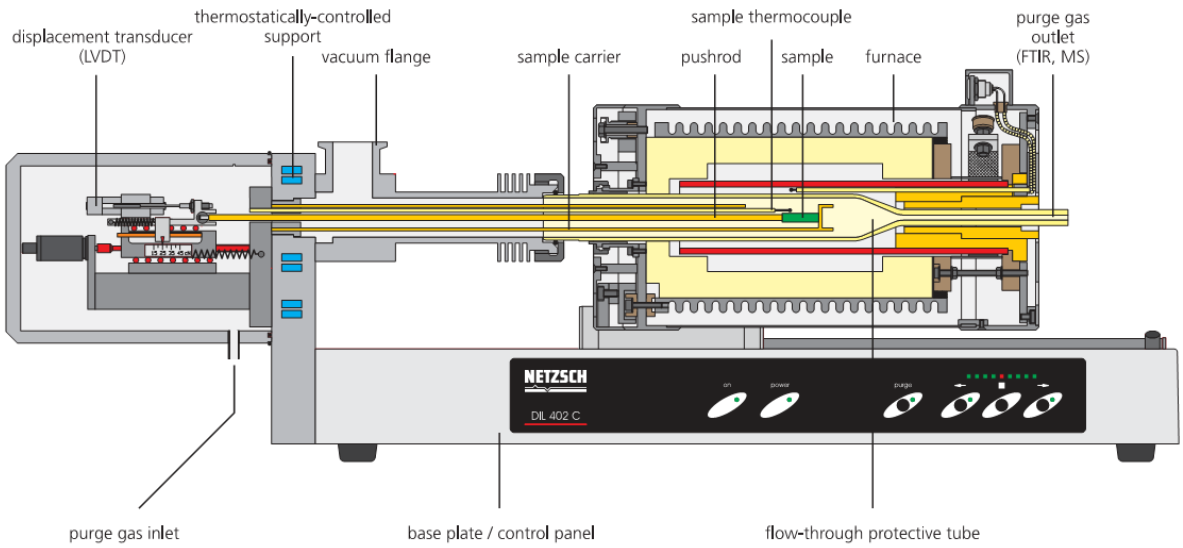

Figure 7 Schematic drawing of a Netzsch DIL 402 C[31]

By pressing an alumina rod on to the sample while carefully controlling and recording the temperature at the end of the push rod, thermal elongation characteristics can be determined. The Linear Variable Displacement Transducer (LVDT) converts the pushrod displacement in to a voltage, and is recorded by software. Since also the sample holder and the pushrod are affected by temperature, it is important to run a background or a correction run if thermal expansion coefficient is to be measured. This is done by inserting a standard pre-sintered sample with known thermal expansion characteristics. After completing the correction run, the sample of interest is inserted and is subjected to the same conditions as the standard. The expansion in the dilatometer is subtracted from the measurement [32].

The data is plotted as shrinkage divided by the initial length against temperature. Shrinkage of the sample is associated by rearrangement of the powder and densification. The dilatometer measurements are divided in two segments, heating and cooling. The heating curve is also referred to as the sintering curve. By evaluating the first derivative of the sintering curve, the optimal sintering temperature and on-set temperature for sintering can be determined. The on-set temperature is the temperature where the slope starts to drop, and shrinkage is observed. These results play an important role in constructing the best sintering program for the material of interest.

Materials expand or contract as a function of temperature. If different materials are in contact during a high temperature processes, possible risk of thermal stress and cracking can occur due to the difference in thermal expansion. Thermal expansion coefficient can be calculated from the slope of the cooling curve obtained in the dilatometer measurements.

2.3.4 BET

The principle behind surface area measurements is based on physisorption of an inert gas such as nitrogen, argon or krypton. The amount of gas covering the surface of a specimen in a monolayer is easily transferred in to a total surface area, if the temperature and diameter of the gas molecule is known. For nitrogen, the gas molecule occupies 0,162 nm^2 at 77 K.
The BET method (Brunauer, Emmett and Teller) [33] determinates the surface area of a specimen by measuring the adsorption-desorption isotherm, and is an extension of the Langmuir isotherm. A type II adsorption isotherm presented in Figure 8, and shows how the amount of adsorbed gas depends on the equilibrium pressure of the gas at constant temperature.

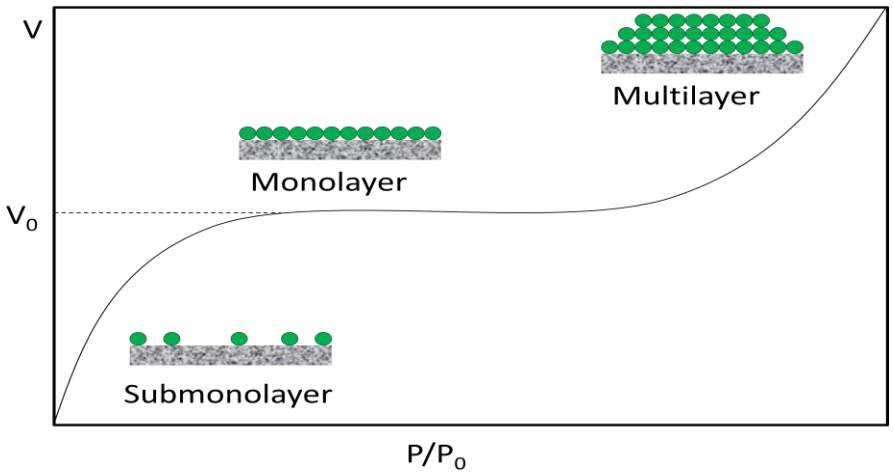

Figure 8 Multilayer adsorption isotherm, modified from [34]

The surface area can be calculated with the equation given in 2.10, also known as the BET equation. Further reading and derivation of the BET equation can be found in [33].

$$\frac{P}{V_a(P_0 - P)} = \frac{1}{\chi V_0} + \frac{(\chi - 1)}{\chi V_0}\frac{P}{P_0} \tag{2.10}$$

Where $\chi = k_1/k$ ratio between adsorption heats of first and next molecular layer, P is the adsorption pressure, P_0 is equilibrium pressure of the condensed gas (saturation pressure), V_a is the total volume of adsorbed gas and V_0 is the volume of gas adsorbed in the first monolayer.

Note that the BET method is valid under the following assumptions:

1. The rate of adsorption and desorption in any layer are equal (equilibrium)
2. In the first layer molecules adsorb on equivalent adsorption sites
3. ΔH_{ads} for the second and consecutive layers are the same. This adsorption heat is approximately equal to the condensation heat of the gas. ($E_{d,2}=E_{d,3}=\ldots=E_{d,i}$)
4. ΔH_{ads} for the first layer is independent of layer 2 and the consecutive layers. $k_1 \neq k_2$
5. The surface is constant during the adsorption

2.4 Sintering

The densification of a particulate ceramic component is typically referred to as sintering. The following criteria must the met before sintering can occur:

1. A mechanism for material transport must be present.
2. A source of energy to activate and sustain material transport must be present.

Sintering is often divided in stages according to physical changes that occur during the process. The different stages and primary physical changes in each step are listed in Table 3.

Table 3 Stages in sintering and physical changes[25]

1st Stage (Initial)	Rearrangement
	Neck formation
2nd Stage (Intermediate)	Neck growth
	Grain growth
	High Shrinkage
	Pore phase continuous
3rd Stage (Final)	Much grain growth
	Discontinuous pore phase
	Grain boundary pores eliminated

There are different types of sintering, but solid-state sintering will be the focus in this report. Solid state sintering involves material transport by volume diffusion. Diffusion can consist of movement of atoms or vacancies along a surface, grain boundary or through the volume of the material. Volume diffusion along grain boundaries or through lattice dislocations results in shrinkage [25].

The primary driving force for densification of a compacted powder at high temperature is the change in surface free energy. Very small particles have high surface free energy and thus have a strong thermodynamically drive to decrease their surface area and bond together. Typically, the finer the powder, the greater the surface area and lower sintering temperature and time at this temperature is needed for densification [25].

The pore structures in the different sintering stages are visualized in Figure 9. As the process continues from point contact to final stage, the pores shrinks and become smoother and more spherical. The intermediate step is the most important for densification and the driving force is elimination of surface energy.

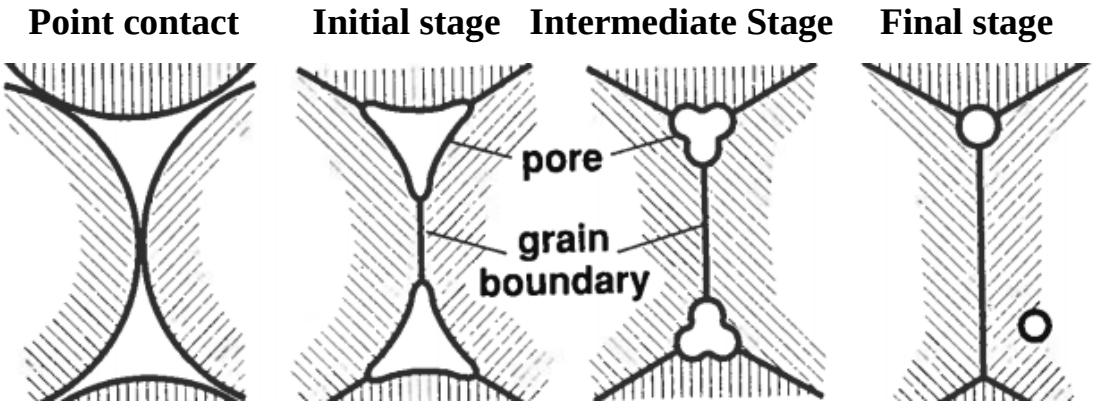

Figure 9 Schematic diagrams of pore structure during sintering[35]

In order to separate hydrogen from other gaseous species, elimination of open porosity is essential in dense ceramic membranes. If open porosity is present, unwanted gas can flow freely from the feed side to the permeate side and hydrogen separation is impossible. It is therefore vital to enter the 3rd and final stage in the sintering to eliminate the continuous pore phase. It is not a dramatic shift where the pores become closed as an indication of the final sintering stage, but a continuous process. The theoretical expectation is that cylindrical pores on the edge of a tetrakaidecahedron, will be instable when the residual porosity falls below 8%, and start to close. Since there is a distribution in grain sizes and pore sizes, normally pores start to close at about 15% porosity and are all closed by 5% porosity [35].

2.4.1 Hot pressing

Hot pressing is a sintering technique that uses both pressure and temperature to activate and sustain material transport. The applied pressure increases the contact stress between the particles, and the available energy for densification is increased by a factor of 20 or more compared to conventional sintering [25]. With the simultaneous application of both pressure and temperature, dense ceramics can be obtained at lower temperatures. The relative low temperature limits the grain growth, and yields a fine microstructure. Due to the applied pressure, voids and pores in the material collapse and higher densities can be achieved compared to conventional sintering [36].

2.4.2 Archimedes principple

The density of refractory materials can be measured using ISO 5017 [37], which is based on Archimedes principle. The principle is built upon the buoyancy of an object with known theoretical density, submerged in a liquid with known density. By measuring the weight of the sample in wet, dry and submerged condition the bulk density, apparent porosity and true porosity can be determined, according to equation 2.12-2.15. Theoretical density is calculated by equation 2.16.

$$\rho_b = \frac{m_1}{m_3 - m_2} \times \rho_{liq} \tag{2.12}$$

$$\pi_a = \frac{m_3 - m_1}{m_3 - m_2} \times 100 \tag{2.13}$$

$$\pi_t = \frac{\rho_t - \rho_b}{\rho_t} \times 100 \tag{2.14}$$

$$\pi_f = \pi_t - \pi_a \tag{2.15}$$

Where ρ_b is the bulk density, ρ_{liq} is the density of the liquid, ρ_t is the true density, π_a is the apparent porosity, π_t is the true porosity and π_f is the open porosity. m_1, m_2 and m_3 is the weight of the sample dry, immersed and soaked respectively.

$$\rho = \frac{m}{V} = \frac{\frac{Z \times M}{A}}{a \times b \times c} \tag{2.16}$$

Where m is the mass in g, V is the volume in cm^3, Z is the number of atoms pr. Unit cell, M is the molar mass, A is Avogadro's number and a,b,c is lattice parameters.

3. Experimentally

3.1 Powder Synthesis

3.1.1 Pechini method

SCZT, SCZYb, SCZY, SCZ, SZ and SC powder were synthesized by the Pechini method, as described in chapter 2.2.1. Aqueous solutions of Cerium Nitrate and Zirconium Nitrate were thermo gravimetrically standardized (1000 ˚C, 3 h) and mixed with dried (110 ˚C, 24 h) Strontium Nitrate. Thulium Nitrate, Ytterbium Nitrate or Yttrium Nitrate was added to substitute cerium at B-site in the doped powders. The nitrate solution was mixed and citric acid was added with a mol ratio of 2:1 of total cations. The mixture was heated to 120 ˚C and mixed with a stirrer at 300 rpm for 30 minutes. Ethylene glycol was added to the mixture with the same 2:1 cation ratio and the mixture was stirred another 30 minutes at 120 ˚C. The mixture was left at room temperature over night and heated stepwise to polyesterification occurred. The gel self-ignited at 300 ˚C and the powder was crushed down in a mortar before calcination. Chemical details are presented in Table 4.

Table 4 Chemical composition, fabricant and purity

Chemical	**Composition**	**Manufacture**	**Purity**
Cerium Nitrate	$CeN_3O_9 \cdot 6H_2O$	Fluka	99,0%
Zirconium Nitrate	$N_2O_7Zr \cdot xH_2O$	Aldrich	99%
Strontium Nitrate	$Sr(NO_3)_2$	Sigma-Aldrich	99,9%
Thulium Nitrate	$N_3O_9Tm \cdot 5H_2O$	Aldrich	99,9%
Ytterbium Nitrate	$N_3O_9Yb \cdot 5H_2O$	Aldrich	99,9%
Yttrium Nitrate	$N_3O_9Y \cdot 5H_2O$	Aldrich	99,9%
Citric acid	$C_6H_8O_7$	VWR	99,5%
Ethylene glycol	$C_2H_6O_2$	VWR	98,0%

3.1.2 Calcination

SC and SZ were calcinated at 1000 ˚C, 1100 ˚C and 1200 ˚C (Naberterm P330 and Labstar 1200/4) for 6 hours in alumina crucibles in ambient air. The heating program for 1000 ˚C is shown in Figure 10. The other programs had the same heating rate and dwell time, but a higher dwell temperature. SCZT, SCZY, SCZYb and SCZ were calcined at 1000 ˚C (Naberterm P330).

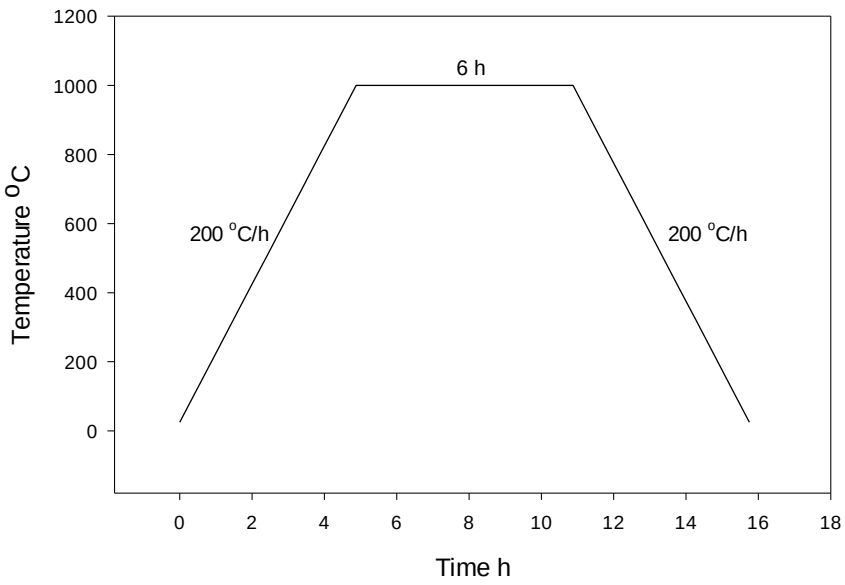

Figure 10 Heat program for calcination at 1000 ˚C

Due to formation of $SrCO_3$ a batch of SCZT was calcined in a tube furnace (Entech ETF30-50/17S) under argon (5.0) flow to reduce the partial pressure of CO_2 (pCO2) to <0,2 Pa [38]. The Same ramp rates and dwell time as in previous calcinations programs was applied, with a dwell temperature of 1200 ˚C.

3.1.3 Ball milling

The powders were milled using a wet ball milling technique. The milling media was alumina balls and isopropanol was used as solvent. The powder was milled for 6 hours or 24 hours. The solvent was evaporated using a rotovapor (Buchi, R-210) at 48 ˚C with a pressure of 69 mbar. The powder was also dried at 400 ˚C for 12 hours (Entech SF-4) to ensure removal of all organics.

3.2 Powder characterization

3.2.1 X-ray Diffraction

X-ray Diffraction (XRD) was carried out on a Siemens D5005 or AXS D8Focus, to determine phase purity of all powders and sintered specimens. The X-ray source is Cu K_α in both XRDs. The program parameters were taken from previous experiments with $SrCeO_3$ [21], with 2θ from 20 to 70 degrees, step size of 0,0200 and 2500 steps. The total time for one continuous scan was 41 min and 41 seconds. All peaks were identified in Eva 2.0 software and lattice parameters were determined by the Reitveld method, in the specimens sintered at 1600 ˚C using TOPAS R software.

3.2.2 Dilatometry

The dilatometer measurements were performed at a Netzsch DIL 402 C. Samples of SCZ, SCZY, SCZYb and SCZT, milled and not milled powders, were prepared by uniaxial pressing using a 5 $mm^{Ø}$ die and an applied pressure of 60 Mpa. Alumina sample holders and spacers were used as support in the dilatometer. A correction run with a pre-sintered alumina standard rod (25 mm) was carried out to eliminate thermal expansion of the system. The correction run was subtracted from the sample data. The experiment was carried out in synthetic air (YaraPraxair, 5.0) [39] at a flow rate of 30 ml/min and a heat and cooling rate of 2 K/min from room temperature to 1500 ˚C. The push-rod applied a constant force of 0,2 N on the samples during the experiment.

3.2.3 Scanning Electron Microscope (SEM)

The powder (milled and not milled) morphology and surface of sintered specimens were investigated in a low-vacuum SEM (Hitachi S-3400N). The samples were coated with gold, using an Edwards sputter coater S150B, due to insufficient electric conductivity of the material at room temperature. Different conditions and parameters were used during imaging, and are presented on the respective photos in Figure 23, 24 and 25.

3.2.4 BET

The surface area of the milled and not milled SCZT was determined by the BET method using a Tristar 3000 from Micromeritics. First a 24 hour degassing step at 250 ˚C was executed to ensure a completely dry powder. The sample was then mounted in the analyzer and the measurement was conducted at 77 K. Nitrogen was used as inert gas.

3.3 Sintering

3.3.1 Conventional sintering

Pellets of 10 mm or 15 mm in diameter were uniaxially pressed and sintered at 1500 ˚C, 1600 ˚C or 1700 ˚C (Entech-01 and Entech HT-2) in ambient air, using a conventional sintering technique. The sintering program for 1600 ˚C is presented in Figure 11. An isothermal step at 1000 ˚C with a dwell time of 6 hours was implemented for degassing of $SrCO_3$.

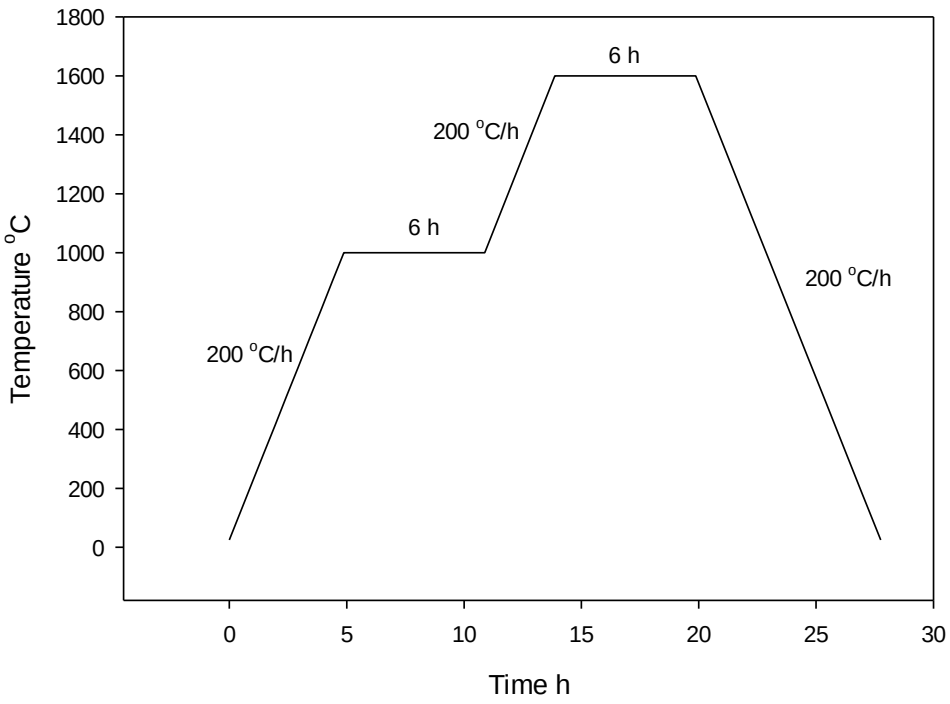

Figure 11 Sintering program at 1600 ˚C

The samples were placed on an alumina disc with a powder bed of SC to reduce reaction with the alumina and minimize friction. An alumina crucible covered the samples. The specimens sintered at 1500 ˚C also had a uniaxial pressed thin disc of the same material as support, to eliminate cation diffusion.

3.3.2 Hot pressing

Hot pressing was conducted at a thermal technology HP50-7010G. The powder was weighed and inserted in a 15 mm carbon die. Carbon spacers between the die and powder were inserted and sprayed with pyrolytic boron nitride to prevent the powder from sticking and possible interactions between the carbon die and powder. The powder was uniaxially pressed with a pressure of 50 Mpa before sintering. Due to inconsistency in temperature between the furnace and the controller, a graph was used to set the right sintering temperature. Argon gas (5.0) at atmospheric pressure was used to limit the reducing conditions, caused by the carbon die. The sintering program for 1600 ˚C is presented in Figure 12.

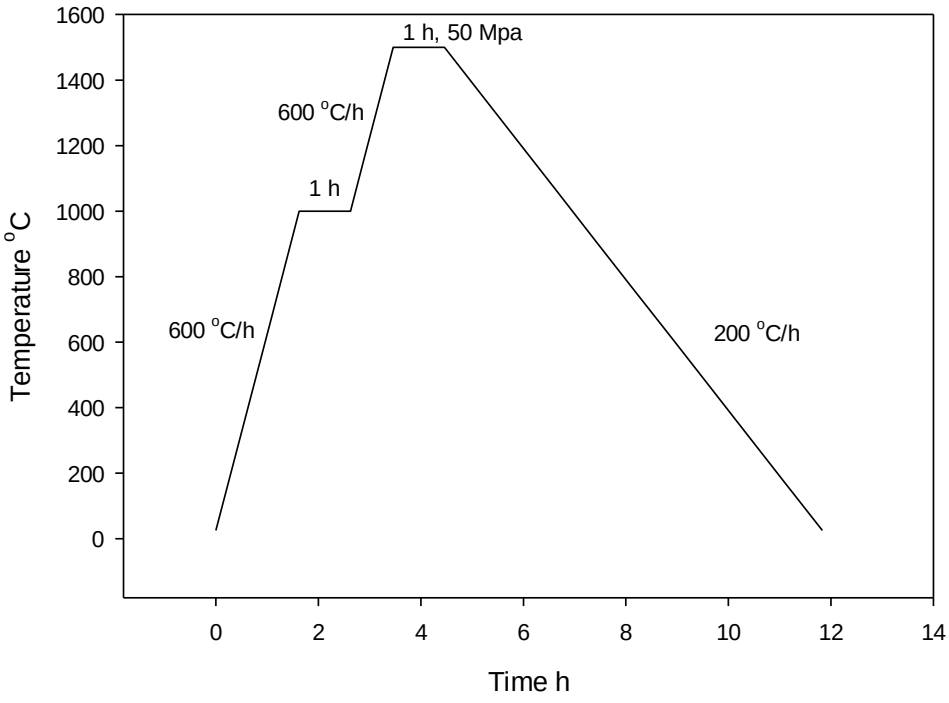

Figure 12 Sintering program for hot pressing

3.3.3 Archimedes principle

The density of the sintered specimens was measured by Archimedes principle and was conducted according to ISO 5017 [37]. Vacuum (15 mBar) was applied to remove air from pores prior to immersion. The samples were submerged in isopropanol, and vacuum was applied for 30 minutes. Submerged samples were weighed when the temperature was stabilized. Density calculations were done according to equation 2.12-2.15 given in chapter 2.4.2.

3.3.4 Grain size

The average grain size in sintered specimens was determined by the liner intercept method as proposed by Mendelson, 1969 [40]. The average grain size was calculated over a minimum of 50 grain boundaries.

4. Results

4.1 Powder characterization by XRD

To investigate the calcination temperature needed to achieve phase pure powder, SC and SZ powders were calicined at 1000 ˚C, 1100 ˚C and 1200 ˚C. XRD results are presented in Figure 13 and Figure 14. Secondary phases such as CeO_2 and Sr_2CeO_4 represent a significant amount in the SC powder calcined at 1000 ˚C. SZ is almost phase pure at 1000 ˚C, but the XRD plot show traces of ZrO_2 and SrO. It is evident that an increase in calcination temperature reduces the amount of secondary phases in both SC and SZ powders. A narrowing in the peaks and an increase in count is also observed for higher calcination temperatures indicating increased crystallization. SC and SZ are phase pure at 1200 ˚C and 1100 ˚C respectively.

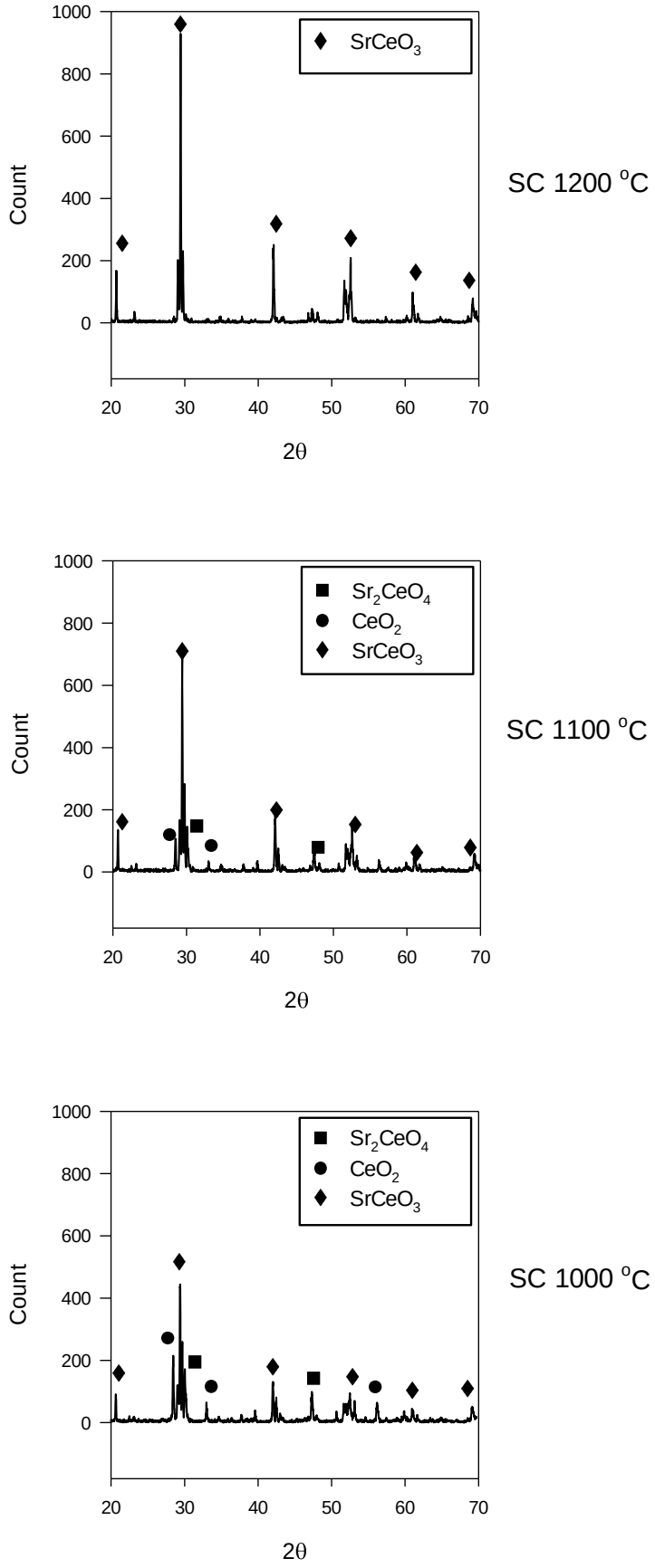

Figure 13 $SrCeO_3$ powder XRD results at 1000 ˚C, 1100 ˚C and 1200 ˚C

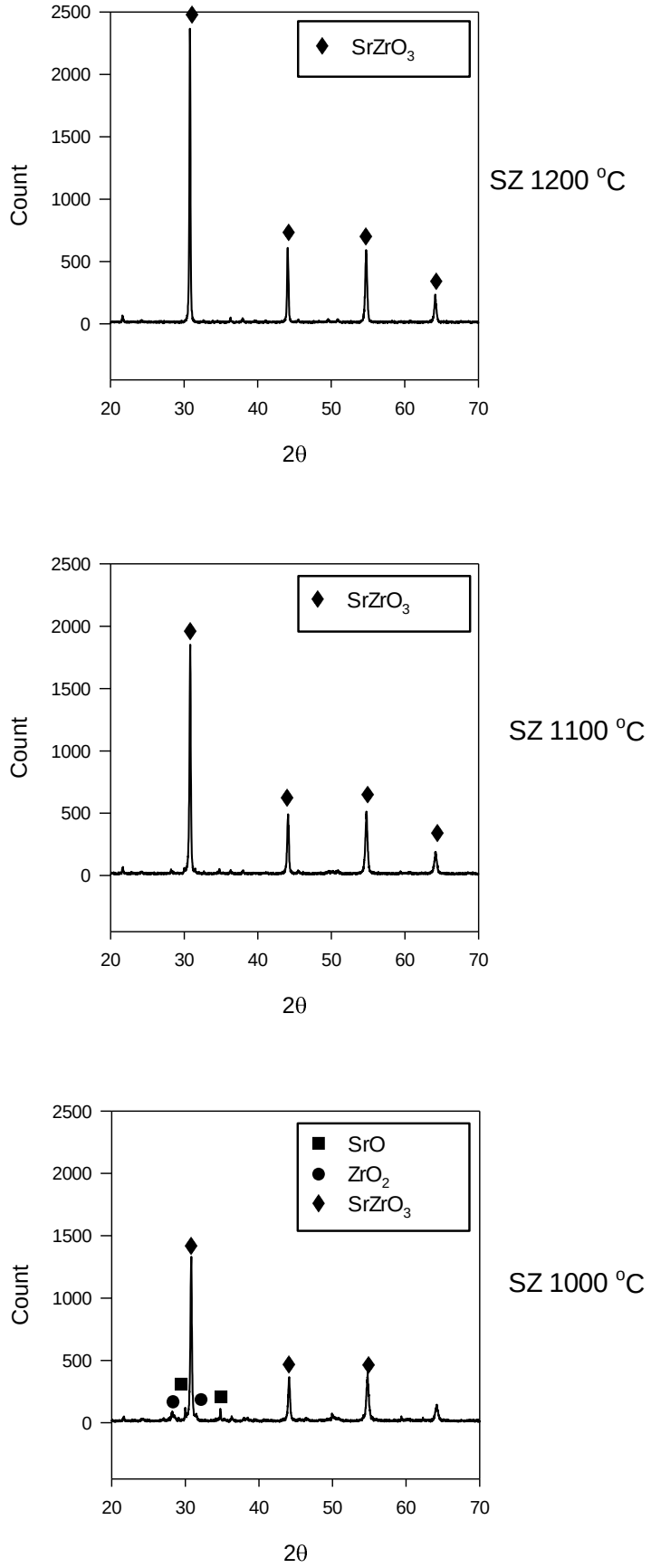

Figure 14 $SrZrO_3$ powder XRD results at 1000 ˚C, 1100 ˚C and 1200 ˚C

When synthesis and calcination of SC and SZ were successful, a test batch of SCZT was prepared. After calcination at 1000 ˚C in air, strontium carbonate was identified at 25 degrees in the XRD plot, in addition to Sr_2CeO_4 and CeO_2. $SrCO_3$ is represented by a ☐ in Figure 15. To eliminate the reaction between $SrCeO_3$ and CO_2, calcination in argon atmosphere at 1200 ˚C was carried out. The significance of the carbonate phase was reduced, but not removed. Secondary phases of Sr_2CeO_4 and CeO_2 are also present at 1200 ˚C. Phase pure SCZT was obtained when a membrane was sintered at 1500 ˚C.

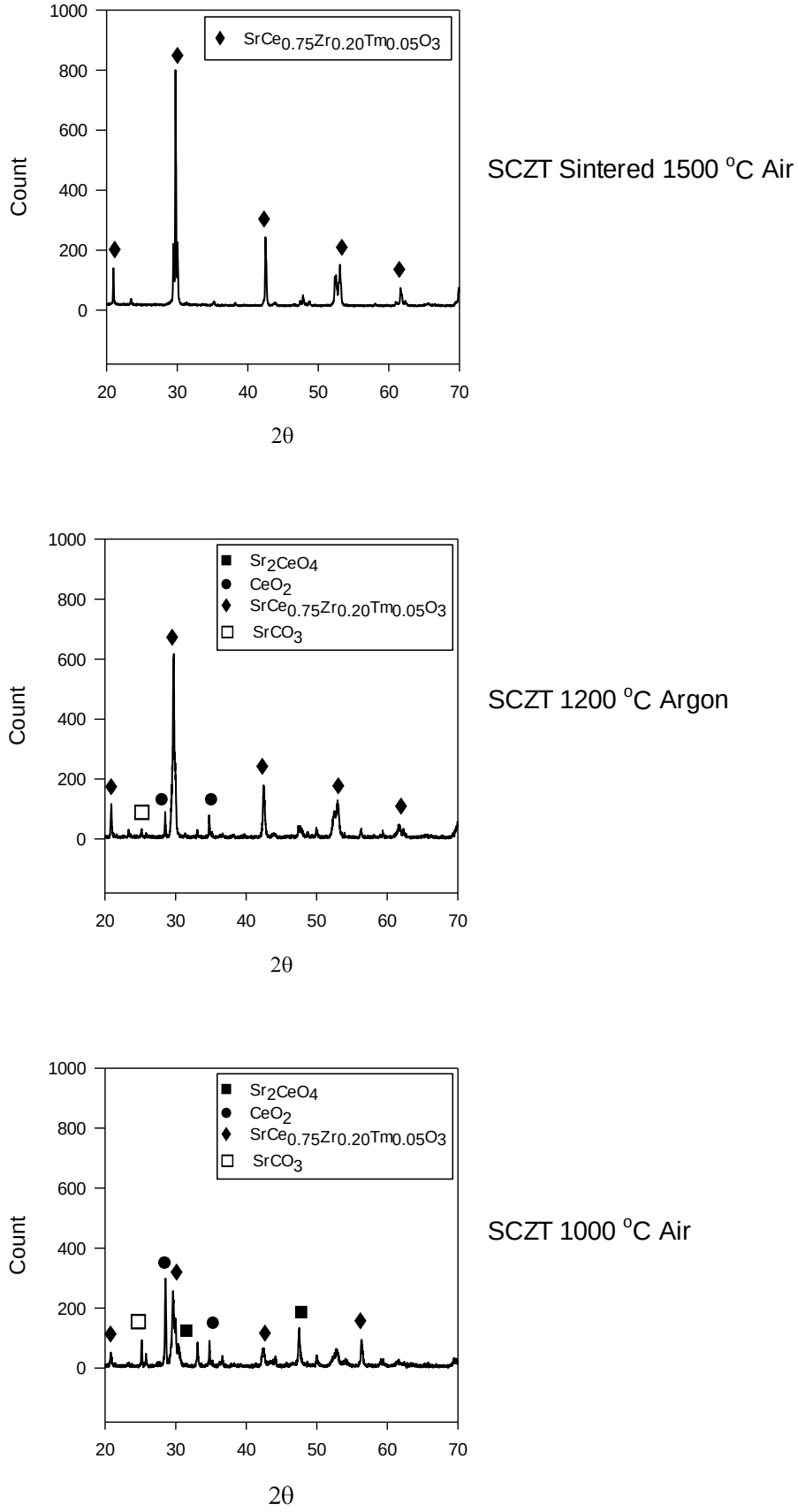

Figure 15 XRD of SCZT at 1000 ˚C in air, 1200 ˚C in argon and sintered at 1500 ˚C in air

Due to initial tests with SC, SZ and SCZT, and the stability of the secondary phases at high calcinations temperatures, the other powders were calcined at 1000 ˚C. The powder XRD of SCZT, SCZY, SCZYb and SCZ is presented in Figure 16. None of the powders are phase pure, but all powders have the same secondary phases as described for SCZT powder, and exhibit similar XRD pattern.

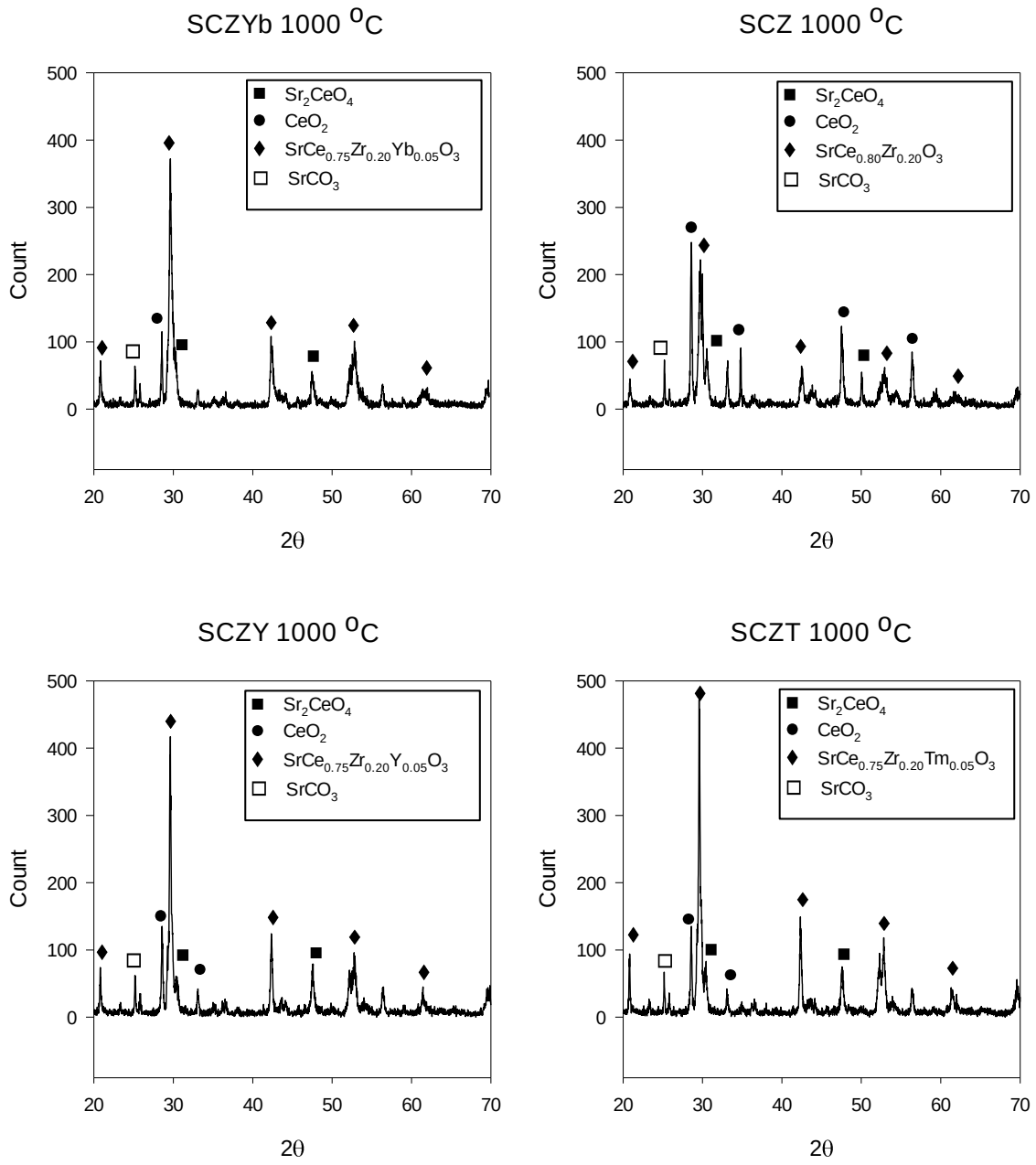

Figure 16 XRD results from powders calcined at 1000 ˚C

The XRD results from samples sintered at 1600 ˚C are showed in Figure 17. All peaks were identified in Eva 2.0 software, showing phase pure orthorombic perovskite structure.

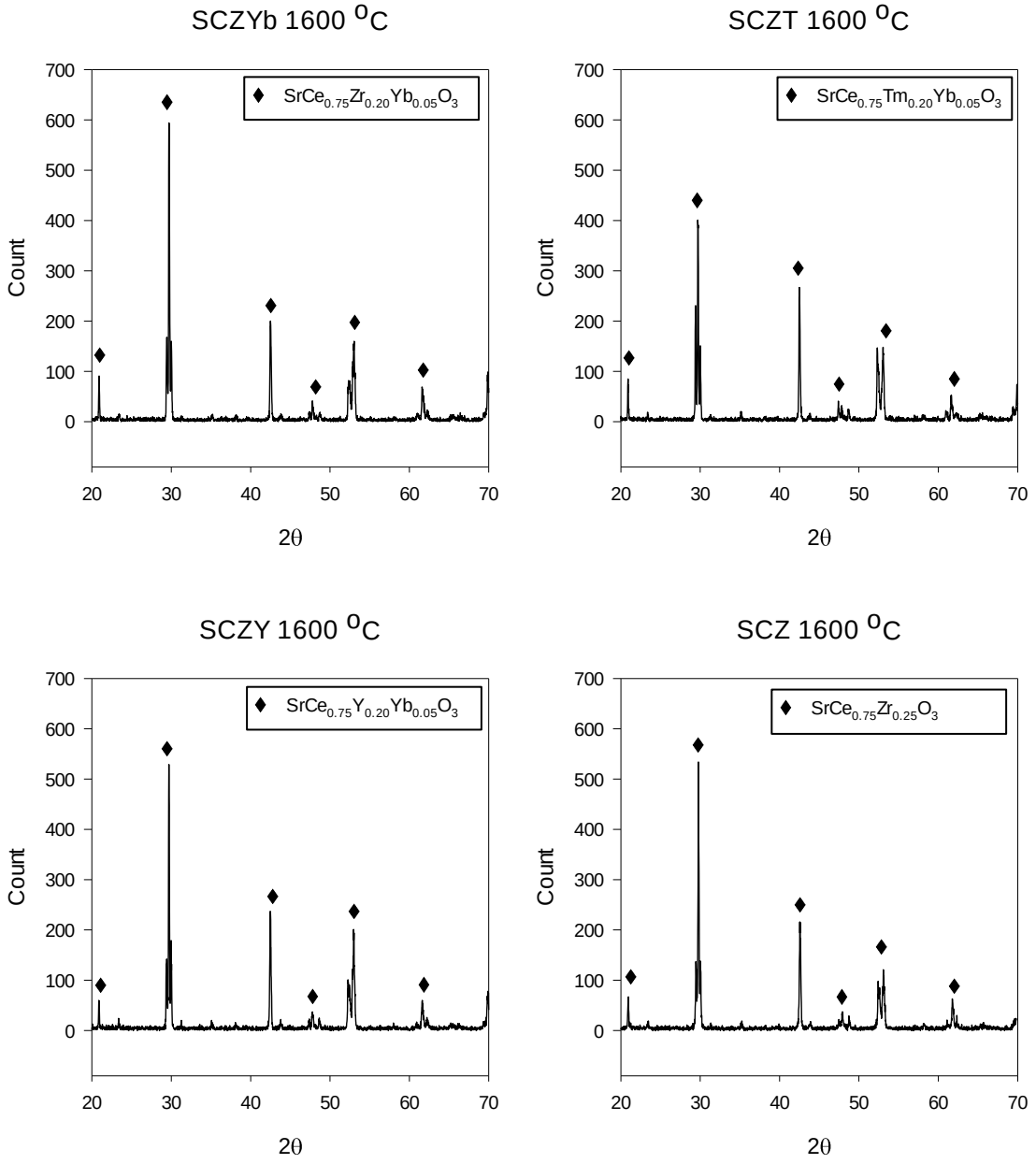

Figure 17 XRD results from samples sintered at 1600 ˚C

Lattice parameters from specimens sintered at 1600 ˚C is presented in Table 5.

Table 5 Lattice parameters of samples sintered at 1600 ˚C, extracted by Topas software

	a [Å]	**b [Å]**	**c [Å]**	**V [Å^3]**	**Theoretical density [g/cm^3]**
SCZ	6,065	8,486	5,955	306,512	5,710
SCZT	6,077	8,509	5,963	308,349	5,760
SCZYb	6,077	8,511	5,965	308,549	5,761
SCZY	6,083	8,511	5,968	308,992	5,662

The above results confirm that Zr^{4+} is dissolved in the SC structure. Theoretical density is calculated according to equation 2.16, given in chapter 2.4.2.

4.2 Dilatometry

Thermal expansion coefficient in the temperature range 40 ˚C-1000 ˚C for SCZT, SCZYb, SCZY and SCZ is presented in Table 6. TEC is calculated from the slope of the dilatometer cooling curves given in appendix A. TEC in other temperature regions are presented in appendix B.

Table 6 Thermal expansion coefficient from 40 ˚C -1000 ˚C

˚C / **TEC 10^{-6}/ ˚C**	**40-1000**
SCZT	12,1
SCZYb	12,1
SCZY	12,4
SCZ	13,0

The dilatometer curve for a pre-sintered (1500 ˚C) SCZT sample with 98,6% density is presented in Figure 18. The difference in length between start and stop is 0,6%, according to data obtained in the dilatometer measurement. TEC during heating and cooling is presented in Table 7. Due to the change in length, density measurements were conducted but minimal change in porosity was demonstrated.

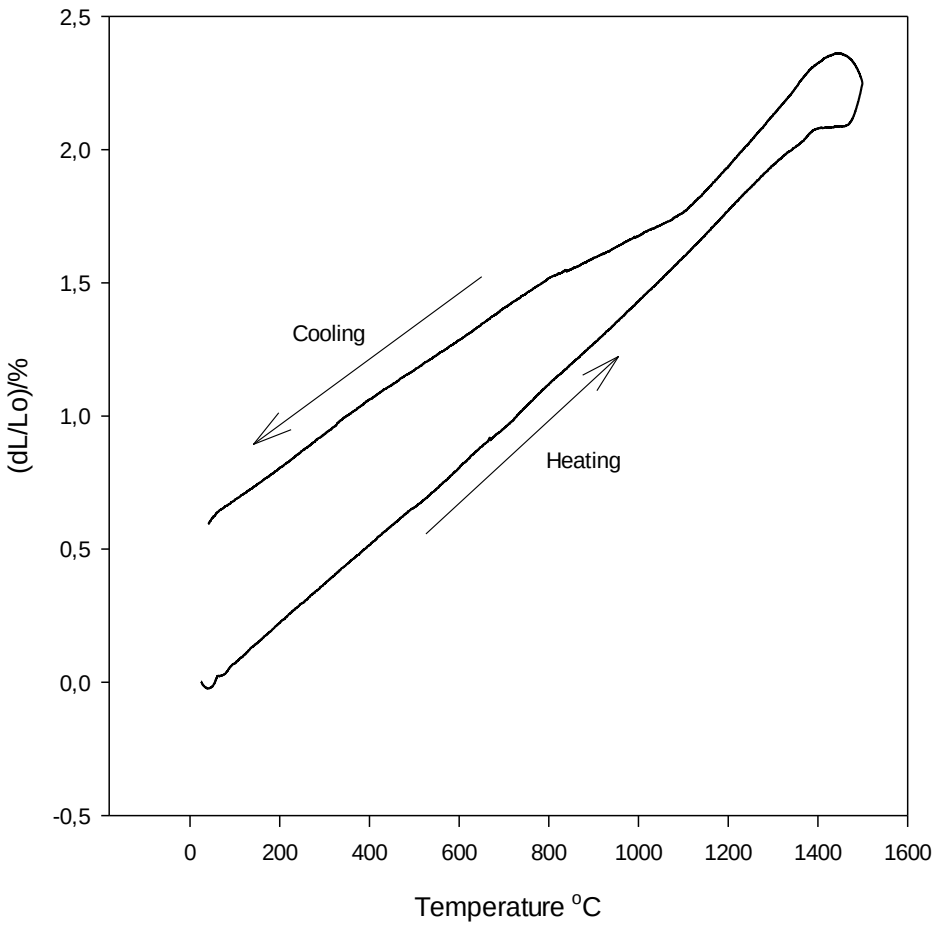

Figure 18 Change in length with respect to initial length of pellet, plotted against temperature, for 1500 ˚C pre-sintered SCZT

Table 7 Thermal expansion coefficient from 40 ˚C-1000 ˚C for pre-sintered SCZT. Separate calculations for heating and cooling curve

˚C / TEC 10^{-6}/ ˚C	40-1000
Heating	15,2
Cooling	11,6

Sintering curves of SCZT, SCZYb, SCZY and SCZ is presented in Figure 19. The samples exhibit close to identical sintering curves. SCZ, represented by the green slope, indicate a lower degree of shrinkage than the other specimens, hence lower densification. Due to the similarity of the sintering curves, SCZT was chosen for further dilatometer analysis regarding milled and not milled powders.

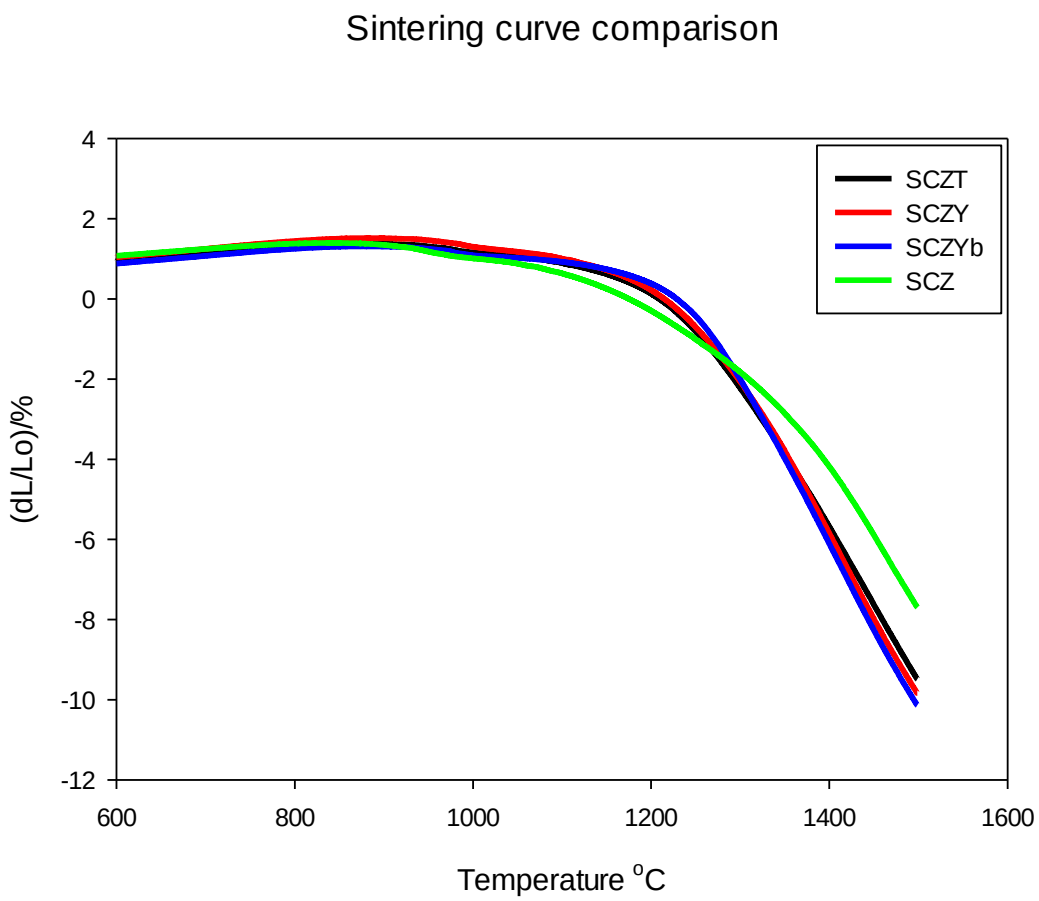

Figure 19 Change in length with respect to initial length of pellet, plotted against temperature. Samples heated to 1500 ˚C from room temperature with 2K/min heat rate

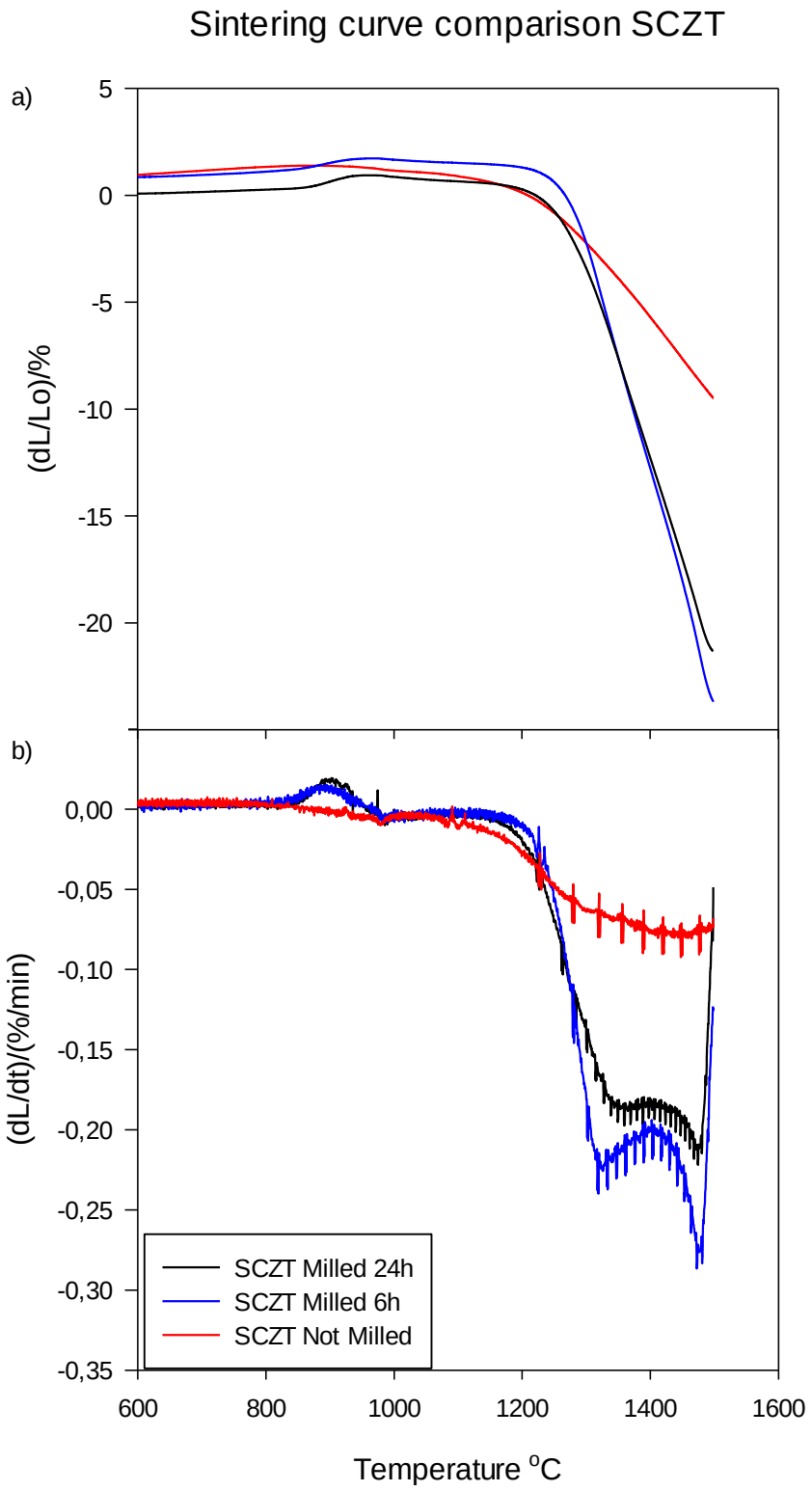

Figure 20 a) Change in length with respect to initial length of pellet, plotted against temperature for milled and not milled SCZT samples. b) First derivative of SCZT sintering curves. Samples heated to 1500 ˚C with 2 K/min heat rate

A comparison of the sintering graphs for milled and not milled SCZT powder is shown in Figure 20 a). After milling for 6 hours the shrinkage of the green body increased from about 13% to 26,75%, compared to the not milled sample. SCZT powder milled for 24 hours resulted in 23% shrinkage with respect to the initial length of the sample.

The first derivative of the sintering curves for milled and not milled SCZT powder is presented in Figure 20 b). The maximum rate of sintering occurs at 1477 ˚C for both of the milled samples. On-set sintering temperature varies from 1250 ˚C to 1277 ˚C for the powder milled 24 and 6 hours, respectively. The 24 hour milled powder show a lower sintering rate than the powder milled for 6 hours at 0,22% and 0,28% per minute respectively. Powder milled for 6 hours are from here on only denoted “milled powder”, unless otherwise specified.

4.3 BET surface area

Surface area of milled and not milled SCZT is presented in Table 8. It is evident that surface area increases with increasing milling time. This is due to the breakdown of larger agglomerates. This is also visualized in SEM micrographs presented in
Figure 21.

Table 8 BET surface area

Sample	**Surface area**
SCZT Not milled	2.0815 $m^2/g \pm 0.0027$ m^2/g
SCZT Milled 6 hours	4.3120 $m^2/g \pm 0.0098$ m^2/g
SCZT Milled 24 hours	6.0135 $m^2/g \pm 0.0108$ m^2/g

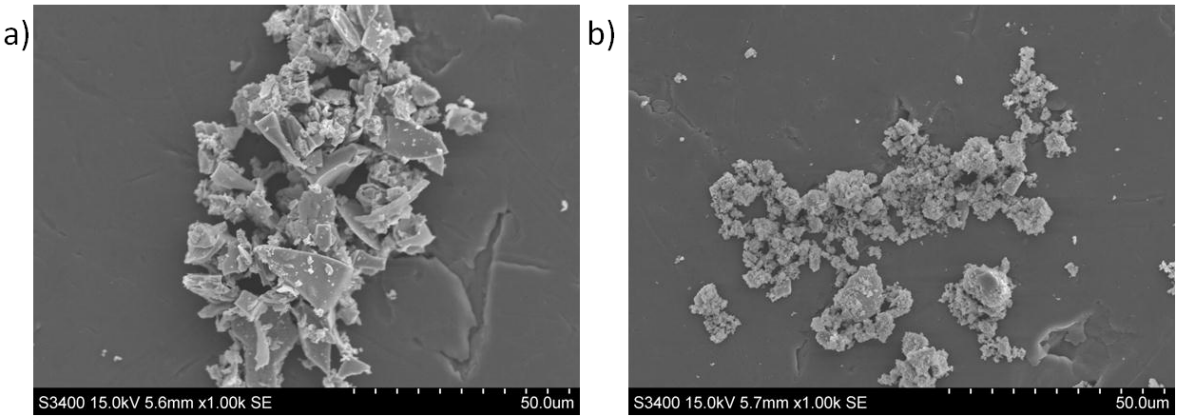

Figure 21 SEM micrograph of a) not milled and b) powder milled for 6 hours

4.4 Density measurements

Density, open porosity and closed porosity of samples sintered at 1500 ˚C or 1600 ˚C with milled and not milled powder, is presented in Table 9. Samples with milled powder sintered at 1500 ˚C show the highest density. SCZT clearly have the highest density, followed by SCZYb, SCZY and SCZ in descending order. SCZ demonstrate a significant decrease in open porosity from 1500 ˚C to 1600 ˚C. Negligible open porosity in SCZT, SCZY and SCZYb sintered with milled powder at 1500 ˚C and 1600 ˚C. Little change in closed porosity for SCZY, but a significant increase in SCZT and SCZYb is observed from 1500 ˚C to 1600 ˚C.

Samples sintered for 1600 ˚C made of not milled powder exhibit lower density and higher open porosity compared to samples made with milled powder. SCZ demonstrate a density of 68,1% and an open porosity of 31,0%, which is significantly lower than the samples with additional doping. Spreadsheet of the density calculations is given in Appendix F.

Table 9 Density, open porosity and closed porosity of samples sintered at 1500 ˚C or 1600˚C.

1500 ˚C Milled	**Density %**	**Open porosity %**	**Closed porosity %**
SCZT	98,6	-0,5	1,9
SCZY	90,8	0,6	8,6
SCZYb	92,3	0,3	7,4
SCZ	74,6	25,0	0,4
1600 ˚C Milled			
SCZT	94,8	0,5	4,7
SCZY	91,5	0,6	7,9
SCZYb	84,1	0,3	15,5
SCZ	88,8	0,3	10,9
1600 ˚C Not Milled			
SCZT	82,3	9,0	8,7
SCZY	76,4	22,3	1,3
SCZYb	79,8	17,3	2,9
SCZ	68,1	31,0	0,8

4.4.1 Hot pressing

Due to the initial densification issues with as calcined powder during conventional sintering, hot pressing was carried out on SCZT powder. When the pellet was extracted from the die it adhered to the carbon spacer, even though it was sprayed with pyrolytic boron nitride. After storage inside a desiccator it disintegrated after approximately 10 days. Lowering the sintering temperature from 1500 ˚C to 1400 ˚C resulted in a cracked pellet, which was extremely brittle, but it did not disintegrate. It was difficult to conduct density measurements on the hot pressed samples, due to the brittle nature of the samples. SEM micrograph of SCZT hot pressed at 1400 ˚C with an applied pressure of 50 Mpa is presented in Appendix E.

4.5 Surface characterization

4.5.1 Macro photo

Figure 22 is a macroscopic picture of a SCZT pellet sintered at 1600 ˚C on a SC powder bed. The color is graded from yellow at the bottom to black on the top, possibly due to difference in cation concentration.

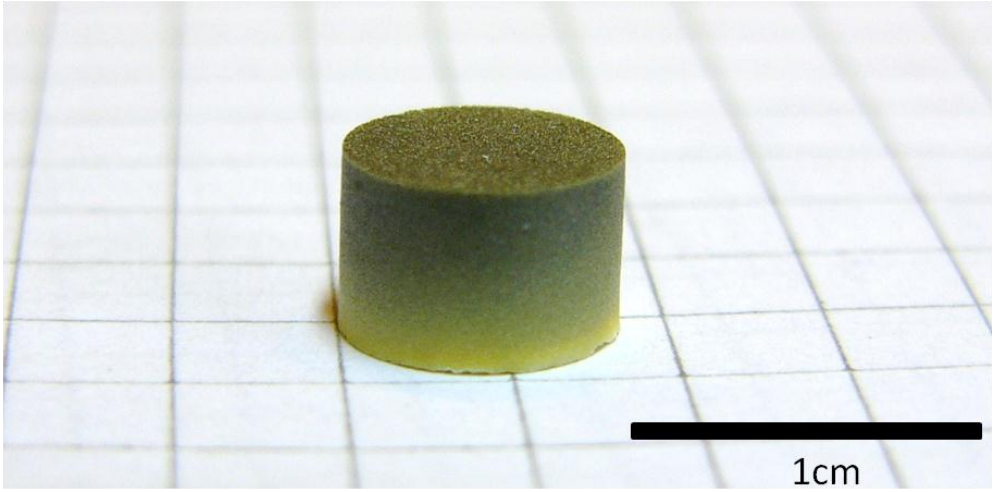

Figure 22 Macro photo of SCZT sintered at 1600 ˚C on SC powder bed

4.5.2 SEM

SEM micrographs of the samples sintered at 1500 ˚C can be viewed in Figure 23, and can give a visual impression of the density measurements and results, presented in Table 9. No porosity is observed in the SCZT surface, represented in Figure 23 c).

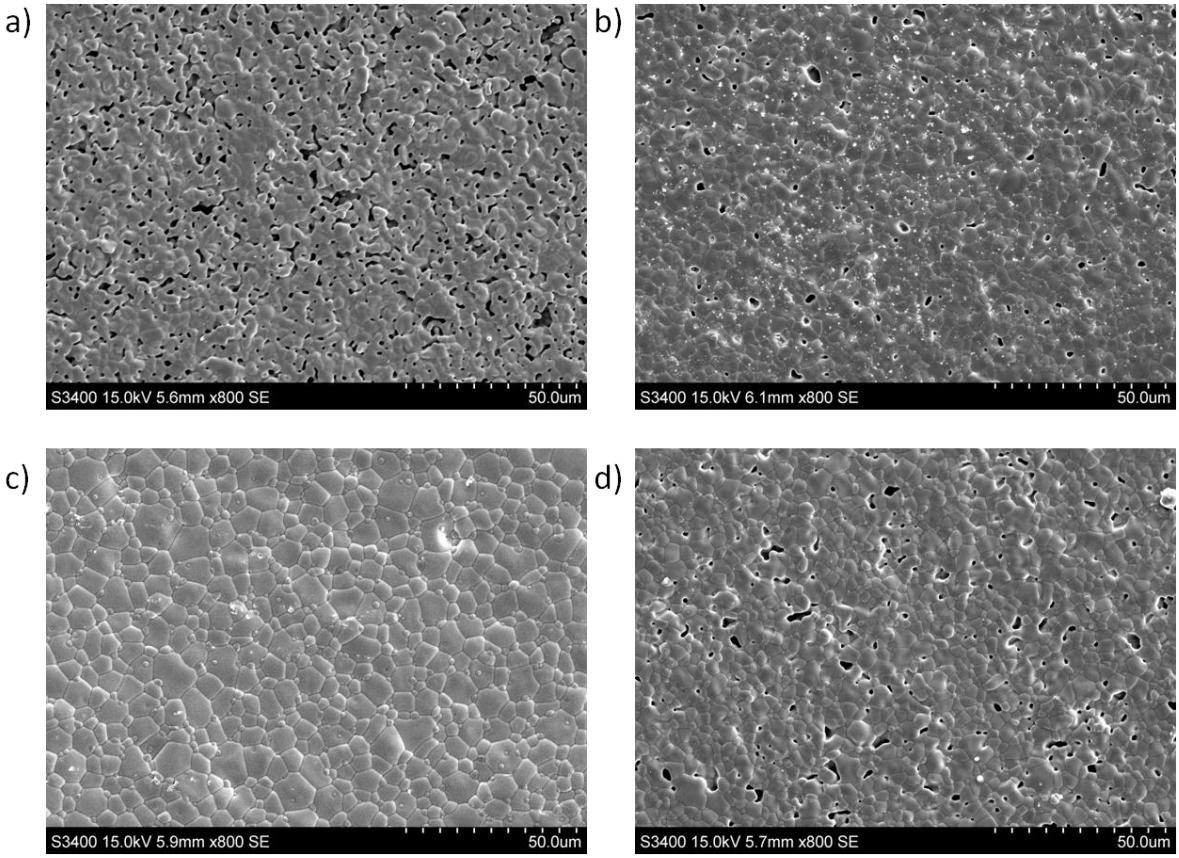

Figure 23 SEM surface micrographs of specimens sintered at 1500 ˚C, milled powder. a) SCZ, b) SCZYb, c) SCZT, d) SCZY

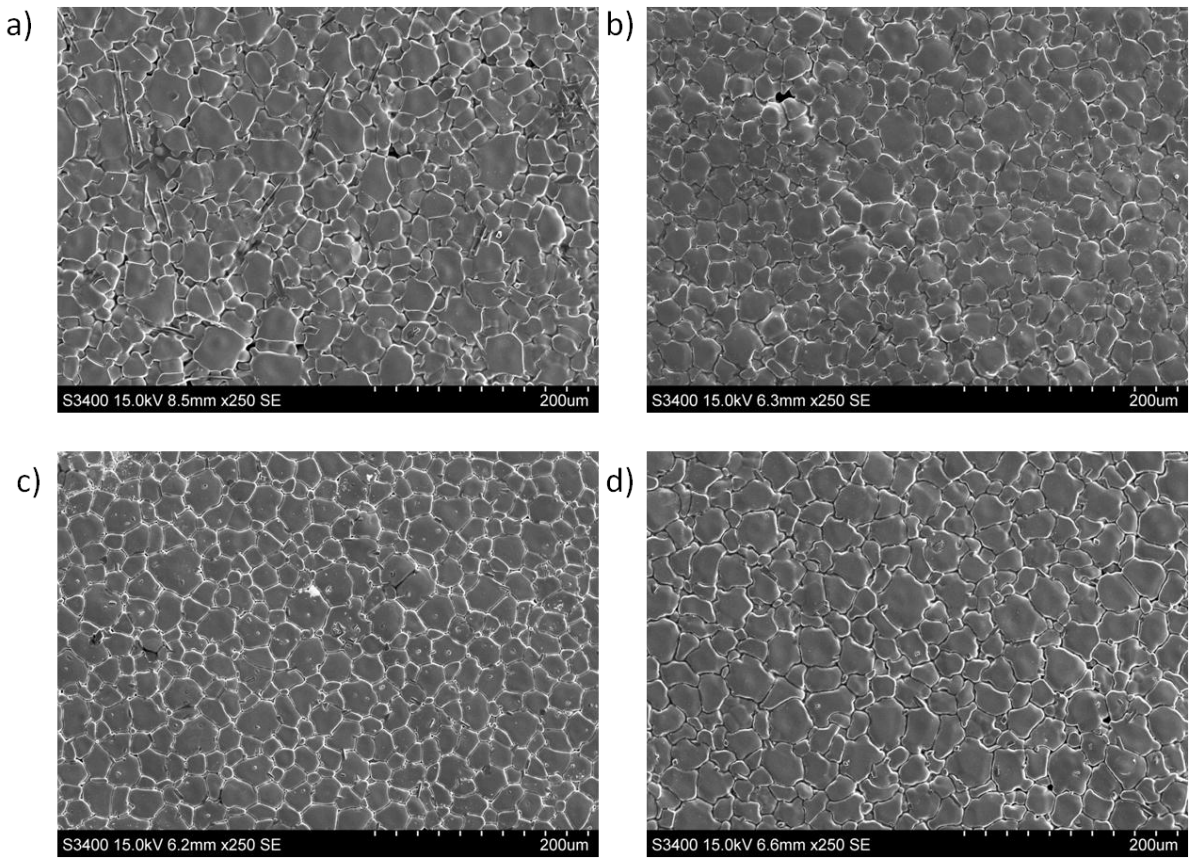

Figure 24 SEM surface images from samples sintered at 1600 ˚C, milled powder. a) SCZ, b) SCZYb, c) SCZT, d) SCZY

Samples sintered at 1600 ˚C, presented in Figure 24, exhibit large grain growth compared to samples sintered at 1500 ˚C. Little or no porosity is visual at the sample surfaces. Note that the length scale is 200 µm, compared to 50 µm in previous micrograph. The average grain size of samples sintered at 1500 ˚C and 1600 ˚C is presented in Table 10.

Table 10 Average grain size for samples sintered at 1600 ˚C

1600 ˚C, milled powder	**Average grain size µm**
SCZ	20,1
SCZYb	20,9
SCZT	19,7
SCZY	22,8
1500 ˚C, milled powder	
SCZ	3,3
SCZYb	3,2
SCZT	4,9
SCZY	3,2

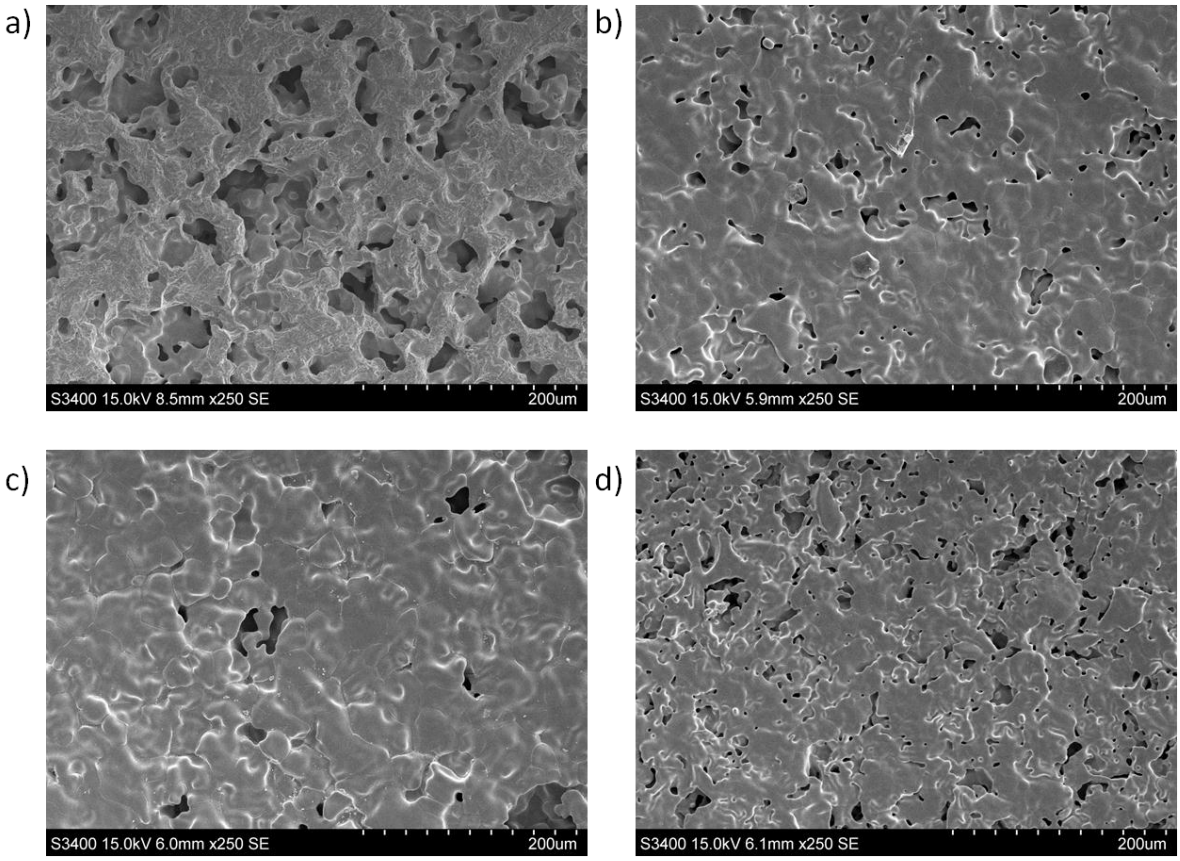

Figure 25 SEM surface micrographs of samples sintered at 1600 ˚C, not milled powder. a) SCZ, b) SCZYb, c) SCZT, d) SCZY

SEM micrographs of samples sintered at 1600 ˚C with not milled powders are presented in Figure 25. It is clear from the pictures that all samples, more or less, exhibit open porosity. The microstructure of the samples varies a lot, compared to each other and compared to the samples made of milled powder and sintered at the same temperature. It was difficult to estimate grain size from the presented SEM micrographs.

5. Discussion

5.1 Powder synthesis and phase purity

The first synthesis of SC and SZ was test batches, intended for learning the synthesis route and determine the calcination temperature. From the powder XRDs it appears that SZ is easier to synthesis, with less secondary phases and required a lower calcination temperature to become phase pure. Since the first batches were small and yielded little powder, it was harder to achieve the exact stoichiometric ratio between the metal nitrates, and hence obtain single phase oxide of desired stoichiometry. This may also explain some problems regarding the phase purity of SC. The same powder was used to investigate different calcination temperatures.

After successful synthesis of SC and SZ, SCZT was synthesized after the same procedure. Calcination in argon atmosphere was carried out, as $SrCO_3$ are expected to form upon cooling in the presence of CO_2 (from air), according to equation 2.7. The XRD results after calcination at 1200 ˚C in argon indicated that although the amount of $SrCO_3$ was reduced, a significant amount was still present. This is in agreement with the equilibrium curves, for equation 2.7, as a function of pCO_2, as defined by Kreuer [16]. The equilibrium curve is presented in Appendix B.

Powder XRD from SCZT, SCZY, SCZYb and SCZ show a variety of phases. The most critical phase present is $SrCO_3$, which resulted in changing the calcination atmosphere to argon. Due to the positive XRD results from the samples sintered at 1500 ˚C and 1600 ˚C, discussed later, nothing further was done to remove these phases from the prepared powders.

A comparison between XRD plot from Liang, J. et al [10] and a XRD plot obtaind from this study is presented in Figure 26. The stoichimetry in the two graphs is identical at x=0.2, and the peak intensities and location of the peaks are comparable. This concludes uniform distribution of Zr and Tm in the lattice.

a)

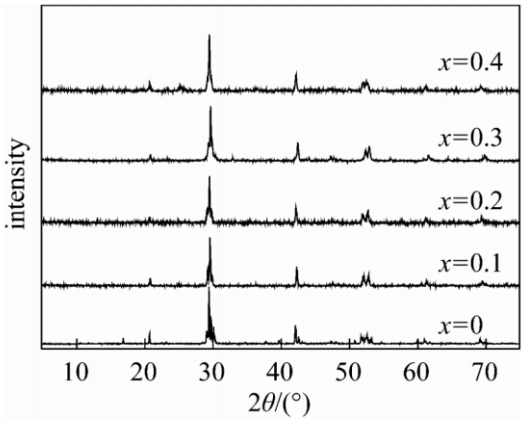

SCZT 1500 Sintered

b)

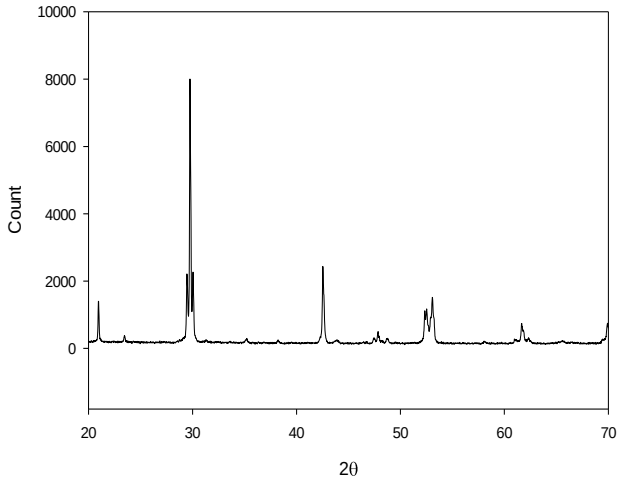

Figure 26 a) XRD plot from Liang, J. et al [10] b) XRD plot from this study

XRD plots presented in Figure 17 clearly exhibit close to identical patterns. The variation in count or intensity at the y-axis in Figure 17 compared to Figure 26 b) is related to different apparatus and the size of the specimens. The area of the incident X-ray beam could exceed the sample area, and the results in Figure 17 are qualitative and only comparable to each other.

Lattice parameters taken from XRD results from specimens sintered at 1600 ˚C, are in agreement with the lattice parameters of SCZT and SCZYb, reported in chapter 2.1.1. Minor differences can be explained by the relative fast XRD scan used in this study. A fast scan is less accurate due to larger θ steps size. The lattice parameters decrease in SCZ compared to the other specimens, and is explained by the difference in ionic radii between Zr^{4+} and Ce^{4+}. Since SCZ have 5 mol% higher zirconium content this was expected and similar trends have been reported in literature [10, 11, 41].

Based on the densification and BET results, as-calcined powders have the tendency to agglomerate and do not demonstrate sufficient density when sintered at 1500 ˚C. Additional milling is needed to obtain dense membranes, but this is normal procedure for powder processing [25].

5.2 Dilatometry

Not milled SCZT, SCZY and SCZYb exhibit almost identical sintering curves. This could be explained by the stoichiometric content of only 5 mol% dopant. The differences between the dopants is however significant with regard to density of sintered specimens. This is discussed in Chapter 5.3. Due to the similarity of the samples, SCZT was the only composition that was investigated by further dilatometer analysis.

The milled SCZT powders showed a clear improvement with regard to densification. Powder ball milled for 6 hours demonstrated a total shrinkage of 27%, compared to 13% for the not milled powder. Powder milled for 24 hours had a total shrinkage of 23%. This result was unexpected as the powder milled for 24 hours had a surface area of 6,01 m^2/g, compared to 4.31 m^2/g for the powder milled for 6 hours. Increased surface area was initially expected to result in higher densification, hence more shrinkage, as seen in the difference between milled and not milled powder in Figure 20 a). However, it should be mentioned that in addition to the breakup of agglomerates the particle size distribution is a key factor for densification [25]. Although the mean particle size was lower for the powder milled for 24 hours, the size distribution of the powder mill for 6 hours could be wider, hence, resulting in improved sintering properties. Another possible reason for the reduced sintering of powder milled for 24 hours could be contamination from the ball milling. Alumina balls were used as milling media, and previous in house research have encountered the same problem. YSZ balls would be the preferred milling media, but it was unavailable at the time.

As mentioned in the theory part, powder with larger surface area usually has a higher sintering rate due to high surface energy. Figure 20 b) deviates from literature, as the sintering rate of powder milled for 24 hours is less than powder milled for 6 hours. The highest sintering rate was measured to 0,28% per minute, at 1470 ˚C for powder milled 6 hours. From practice, oven temperature is set above optimal to sintering temperature, found from dilatometry, to ensure maximum sintering rate. 1500 ˚C was concluded to be sufficient. The on-set sintering temperature was lowered from 1277 ˚C to 1250 ˚C for SCZT powder milled for 24 hours compared to SCZT powder milled for 6 hours. This was expected and is explained by the increase in surface area [25, 35].

The first derivative of the sintering curve also indicate a sintering rate of 0,22% per minute at 1325 ˚C. This is below the maximum sintering rate of 0,28 % per minute, but probably sufficient to obtain dense membranes provided sufficient sintering time is used. A smaller grain size would be expected from a lower sintering temperature.

In the dilatometer test, cylindrical samples with 5 mm^{Ø} had to be used. Due to the insensitive pressure gauge on the uniaxial press, the green body density varies in all specimens, caused by different applied pressure. This might influence the total density and might explain some differences in early stage in the dilatometer measurements, due to rearrangement of the powder. The whole graph from 40 ˚C to 1500 ˚C is presented in Appendix C.

5.2.1 Thermal expansion coefficient

Cooling curves from 1500 ˚C to 40 ˚C, presented Appendix A are the basis for TEC values. The graph was edited due to vertical jumps in the cooling curve. This may be caused by high friction between the sample and sample holder or micro cracks introduced during pressing.

TEC reported in Table 6 is higher than what is reported for SC and SZ, at 11,1 and 9,69 x 10^{-6}/K between 300 K and 1000 K [9, 42]. The trivalent dopants seem to lower the thermal expansion, which is contradicting according to Hassan D. et al. [43]. They report TEC in the range 11,5 – 12 x 10^{-6}/K for ytterbium doped SC and 10,4 x 10^{-6}/K for ytterbium doped SZ, measured at 1000 ˚C. TEC values with 200 ˚C intervals from 40 ˚C to 1200 ˚C are presented in Appendix B. All though the TEC values are uncertain, the general area of 12-15 x 10^{-6}/˚C is established.

Table 7 shows a deviation in TEC between the heating and cooling for pre-sintered SCZT, which is also visualized in Figure 18. Ideally the curve should be identical, and the ending point should be the same as the starting point. From the graph data, an expansion of 0,6% (calculated to 0,03 mm) between start and stop is demonstrated. Density measurements reviled a 0,7% decrease in density, but can be related to uncertainties in the measurement caused by removal of excess isopropanol when weighing wet sample. The difference in expansion between heating and cooling can be detrimental with regard to industrial implementation. Thermal cycling would be expected in an industrial application, due to start and stops in the production. If the expansion in the membrane differs with each cycle, thermal stress and cracking could be induced and result in membrane failure. A more thorough study of thermal cycling would be necessary before too much effort and time is invested in doped SCZ.

5.3 Sintering

The uniaxial pressed green bodies were sintered on an alumina disc, with various supports. Due to temperature gradients in the furnace and the location of the thermo element, the alumina disc was placed at the same location in the furnace to ensure reproducibility. When the pellets were laid on a SC powder bed, color grading was observed as showed in the macro photo in Figure 22. The color grading is most likely caused by cation gradients or difference crystal structure in the sample, and is unwanted. Cerium oxide is known to have a pale yellow color, and is possibly present in the lower part of the membrane [44]. By pressing a disc made of the same powder as the pellet and laying the pellet on top resulted in uniform color. The disc adhered to the pellet, but was easily removed.

Three different sintering temperatures were investigated for not milled SCZT powder; 1500 ˚C, 1600 ˚C and 1700 ˚C. Sintering at 1500 ˚C resulted in a membrane with 68% density, measured by Archimedes method. The membrane sintered at 1600 ˚C also exhibited open porosity by visual investigation. At 1700 ˚C the membrane reacted with the alumina and the SC powder bed, and the temperature was concluded to be too high.

Hot pressing of as calcined SCZT powder resulted in a disintegrated membrane probably due to the formation of carbonates. The reducing conditions inside the carbon die and too high sintering temperature is possible explanations for failure. Lowering the sintering temperature from 1500 ˚C to 1400 ˚C resulted in a cracked pellet, which was extremely brittle, but it did not disintegrate. Further decrease in sintering temperature and or pressure, changing the die material and conduct pressing with milled powder may have improved the results, but hot pressing was disregarded after multiple failures.

After milling the density of the conventional sintered membranes increased from 68% to 98,6% for SCZT sintered at 1500 ˚C. SCZY and SCZYb demonstrated a density of 90,8% and 92,3% respectively. According to theory presented in chapter 2.4, no open porosity should be present which is in accordance with the density results presented in Table 9. The membrane density is therefore regarded as sufficient. The optimal sintering temperature was set according to SCZT, on the fact that SCZY and SCZYb had almost similar sintering curves. This have played a role in the supreme density of SCZT compared to the other samples.

Liang, J et.al [10] reported a sintering temperature of 1525 ˚C and 20 hour dwell time, to achieved dense SCZT synthesized by the Pechini method. This study demonstrates a 25 ˚C lower sintering temperature and a 14 hour decrease in sintering time, for obtaining close to theoretical density with reduced grain growth. Solid state synthesis of strontium cerates normally reports highest sintering rate at higher temperatures such as 1600 ˚C [43]. Yamakana, S et.al [9] reports higher density in $SrZrO_3$ (93%) than in $SrCeO_3$ (84%), synthesized by the solid state reaction, sintered at 1500 ˚C.

All pores visible in the surface of SCZYb and SCZY are located at the grain boundaries, which may indicate that the sintering is not complete and hence, a longer dwell time at 1500 ˚C would remove residual closed porosity. Pores located on grain boundaries are visualized in Appendix D. The grain size in SCZY and SCZYb is also smaller than those exhibited by SCZT, which justifies the argument of longer dwell time. This is also in agreement with reported densities of 99% for SCZYb, with 40 mol% zirconium at B-site, sintered at 1500 ˚C for 10 hours [14].

SCZ sintered at 1500 ˚C, demonstrates 25% open porosity and have not entered the final stage in the sintering process. The incorporation of trivalent cations at B-site, clearly have a positive effect on the densification of the membranes. This could be explained by the oxygen vacancies created by incorporation of thulium, ytterbium or yttrium. Sintering rate is limited by diffusion of the slowest-moving-ion, and the oxygen vacancies should lower the activation barrier for diffusion [21].

At 1600 ˚C all samples demonstrate an increase in the closed porosity. This is probably due to exaggerated grain growth, resulting in trapped pores within grains with little driving force for elimination. As seen from Table 9, no or little open porosity is present in milled SCZT, SCZY or SCZYb sintered at 1500 ˚C or 1600 ˚C. This is in agreement with literature, which states that the pores start to close around 85% density and is completely closed at 95% density [35].

Surface micrographs reveal large differences in grain size of the membranes sintered at 1500 ˚C and 1600 ˚C, made of milled powder. Average grain size of the sintered membranes was 3,2 – 4,9 μm at 1500 ˚C and 19,7 – 22,8 μm at 1600 ˚C. The high temperature causes the large grains to grow on the expense of small grains, increasing the average grain size in the membrane. According to Dahl, P.I et.al [21] critical grain size for strontium cerate based materials is ~6-7 μm, to avoid micro cracking and poor mechanical properties. The membranes sintered at 1600 ˚C exceed this limit, and the temperature is therefore regarded as too high.

6. Conclusion

The Pechini method proved itself to be a successful process route for synthesis of dense and homogeneous strontium cerates stabilized with zirconium and doped with thulium, ytterbium or yttrium. The synthesis method required additional milling to achieve sufficient surface area and small particle size, to promote densification.

Milling the powder for 6 hours increased the surface area from 2,08 m^2/g to 4,31 m^2/g. Doped powder calcined at 1000 ˚C in ambient air, milled for 6 hours and sintered at 1500 ˚C demonstrated the sufficient density required for elimination of open porosity. Thulium doped SCZ showed the highest density of 98,6% followed by ytterbium, and yttrium doped SCZ at 92,3% and 90,8% respectively. The addition of thulium, ytterbium and yttrium increased the densification of SCZ significantly, which showed a density of 74,6% and an open porosity of 25% sintered at 1500 ˚C.

The synthesized powders were not phase pure, and the elimination of $SrCO_3$ and CeO_2 was problematic, even in argon atmosphere. After sintering at 1600 ˚C, no secondary phases were detected by X-ray Diffraction and the material exhibited a phase pure orthorhombic perovskite structure.

Grain size in the dense membranes sintered at 1500 ˚C was in the range 3,2 μm – 4,9 μm. Sintering at 1600 ˚C resulted in extensive grain growth, and the temperature is concluded to be too high, with respect to powders synthesized by the Pechini method and milled for 6 hours.

Thermal expansion coefficient from 40 ˚C-1000 ˚C for SCZT, SCZYb, SCZY and SCZ was determined to (12,1, 12,1, 12,4 and 13,0) $\times 10^{-6}$/ ˚C respectively. Variation in TEC between heating and cooling in pre-sintered SCZT cause for a more thorough investigation before determining the exact thermal properties of the membrane.

Further work

It would be interesting to investigate the total conductivity of the different membranes at elevated temperature and different atmospheres. The conductivity is related to the hydrogen flux and is a normal way of ranking hydrogen separation. A comparison of the hydrogen flux for the different membranes is crucial for determining the best hydrogen separation membrane.

It would also be interesting to investigate sintering at 1325 ˚C, and compare it to 1500 ˚C. On the basis of the density results in this report, dilatometer measurements for milled SCZY and SCZYb powder would be valuable. Dilatometer measurements on pre-sintered specimens and cycling effects is also recommended for further investigation before investing more time in producing these membranes.

References

1. Phair, J. and S. Badwal, *Review of proton conductors for hydrogen separation.* Ionics, 2006. **12**(2): p. 103-115.
2. Bernardo, P., E. Drioli, and G. Golemme, *Membrane Gas Separation: A Review/State of the Art.* Industrial & Engineering Chemistry Research, 2009. **48**(10): p. 4638-4663.
3. Hatlevik, Ø., et al., *Palladium and palladium alloy membranes for hydrogen separation and production: History, fabrication strategies, and current performance.* Separation and Purification Technology, 2010. **73**(1): p. 59-64.
4. Iwahara, H., et al., *Proton conduction in sintered oxides and its application to steam electrolysis for hydrogen production.* Solid State Ionics, 1981. **3–4**(0): p. 359-363.
5. Kreuer, K.-D., *Proton Conductivity: Materials and Applications.* Chemistry of Materials, 1996. **8**(3): p. 610-641.
6. Bhalla, A.S., R. Guo, and R. Roy, *The perovskite structure – a review of its role in ceramic science and technology.* Materials Research Innovations, 2000. **4**(1): p. 3-26.
7. Goldschmidt, V.M., *Geochemische Verteilungsgesetze der Elemente*. 1926, Oslo: I kommisjon hos Jacob Dybwad. b.
8. Levy, M.R., *Crystal Structure and Defect Property Predictions in Ceramic Materials*, in *Department of Materials* 2005, Imperial College of Science,Technology and Medicine: London.
9. Yamanaka, S., et al., *Thermophysical Properties of Perovskite-Type Strontium Cerate and Zirconate.* Journal of the American Ceramic Society, 2005. **88**(6): p. 1496-1499.
10. Liang, J., et al., *Protonic and Electronic Conductivities and Hydrogen Permeation of SrCe0.95-xZrxTm0.05O3-δ(0≤x≤0.40) Membrane.* Chinese Journal of Chemical Engineering, 2010. **18**(3): p. 506-510.
11. Matzke, T. and M. Cappadonia, *Proton conductive perovskite solid solutions with enhanced mechanical stability.* Solid State Ionics, 1996. **86–88, Part 1**(0): p. 659-663.
12. Norby, T. and R. Haugsrud, *Dense Ceramic Membranes for Hydrogen Separation*, in *Membranes for Energy Conversion*. 2008, Wiley-VCH Verlag GmbH & Co. KGaA. p. 169-216.
13. Kingery, W.D., H.K. Bowen, and D.R. Uhlmann, *Introduction to ceramics*. 1976, New York: Wiley. xii,1032 s.
14. Zhang, J., et al., *Combustion synthesis and characterization of nanocrystalline proton conducting Sr(Ce0.6Zr0.4)0.95Yb0.05O3−δ.* Journal of Alloys and Compounds, 2009. **473**(1–2): p. 308-313.
15. Scholten, M.J., et al., *Synthesis of strontium and barium cerate and their reaction with carbon dioxide.* Solid State Ionics, 1993. **61**(1–3): p. 83-91.
16. Kreuer, K.D., *On the development of proton conducting materials for technological applications.* Solid State Ionics, 1997. **97**(1–4): p. 1-15.
17. Katahira, K., et al., *Protonic conduction in Zr-substituted BaCeO3.* Solid State Ionics, 2000. **138**(1–2): p. 91-98.
18. Cheng, S., V.K. Gupta, and J.Y.S. Lin, *Synthesis and hydrogen permeation properties of asymmetric proton-conducting ceramic membranes.* Solid State Ionics, 2005. **176**(35–36): p. 2653-2662.

19. Hamakawa, S., et al., *Synthesis and hydrogen permeation properties of membranes based on dense SrCe0.95Yb0.05O3−α thin films.* Solid State Ionics, 2002. **148**(1–2): p. 71-81.
20. Lu, G.Q., et al., *Inorganic membranes for hydrogen production and purification: A critical review and perspective.* Journal of Colloid and Interface Science, 2007. **314**(2): p. 589-603.
21. Dahl, P.I., et al., *Synthesis, densification and electrical properties of strontium cerate ceramics.* Journal of the European Ceramic Society, 2007. **27**(16): p. 4461-4471.
22. Chavan, S.V. and A.K. Tyagi, *Preparation and characterization of Sr0.09Ce0.91O1.91, SrCeO3, and Sr2CeO4 by glycine–nitrate combustion: Crucial role of oxidant-to-fuel ratio.* Journal of Materials Research, 2004. **19**(11): p. 3181-3188.
23. Pechini, M.P., *Method of preparing lead and alkaline earth titanates and niobates and coating method using the same to form a capacitor*, U.S.P. Office, Editor. 1967: USA.
24. Fajardo, H.V., et al., *Synthesis, characterization and catalytic properties of nanocrystaline Y2O3-coated TiO2 in the ethanol dehydration reaction.* Materials Research, 2012: p. 0-0.
25. Richerson, D.W., *Modern Ceramic Engineering*. 3rd ed. 2006, Boca Raton: CRC Press Taylor and Francis Group. 384.
26. West, A.R., *Basic Solid State Chemistry*. Second ed. 1999, Chichester: John Wiley & Sons Ltd.
27. Stanjek, H. and W. Häusler, *Basics of X-ray Diffraction.* Hyperfine Interactions, 2004. **154**(1): p. 107-119.
28. Goldstein, J., Newbury, D.E., Joy, D.C., Lyman, C.E., Echlin, P., Lifshin, E., Sawyer, L., Michael, J.R., *Scanning Electron Microscopy and X-ray Microanalysis*. 3rd ed. 2003, New York: Plenum publishers.
29. Hjelen, J., *Scanning elektron-mikroskopi*. 1989, Trondheim: Metalurgisk institutt, NTH.
30. Sutton, M., et al., *Scanning Electron Microscopy for Quantitative Small and Large Deformation Measurements Part I: SEM Imaging at Magnifications from 200 to 10,000.* Experimental Mechanics, 2007. **47**(6): p. 775-787.
31. Analysis, N.T., *DIL 402 C*, N.-G. GmbH, Editor. 2012: Bavaria.
32. Daw, J.E., et al., *Viability of Pushrod Dilatometry Techniques for High Temperature In-Pile Measurements*. 2008. p. Medium: ED.
33. Brunauer, S., P.H. Emmett, and E. Teller, *Adsorption of Gases in Multimolecular Layers.* Journal of the American Chemical Society, 1938. **60**(2): p. 309-319.
34. Chorkendorff, I. and J.W. Niemantsverdriet, *Concepts of Modern Catalysis and Kinetics*. 2007: Wiley-VCH.
35. German, R.M., *Sintering Theory and Practice*. 1996: Wiley.
36. King, A.G., *Ceramic Technology and Processing*. 2002: Noyes Publications/William Andrew Pub.
37. Standardization, I.O.f., *Dense shaped refractory products -- Determination of bulk density, apparent porosity and true porosity*, in *ISO 5017:1988*. 1988.
38. Obrestad, H., *Salgsspesifikasjon Argon 5.0 Ultra, SS91*. 2011, YaraPraxair.
39. Obrestad, H., *Salgsspesifikasjon Syntetisk luft 5.0 Ultra, SS147*. 2012, YaraPraxair.
40. Mendelson, M.I., *Average Grain Size in Polycrystalline Ceramics.* Journal of the American Ceramic Society, 1969. **52**(8): p. 443-446.

41. Li, J., et al., *Stability of SrCe[sub 1 - x]Zr[sub x]O[sub 3 - delta] under Water Gas Shift Reaction Conditions.* Journal of The Electrochemical Society, 2010. **157**(3): p. B383-B387.
42. Sahu, M., et al., *Heat capacity and thermal expansion coefficient of SrCeO3(s) and Sr2CeO4(s).* Thermochimica Acta, 2011. **525**(1–2): p. 167-176.
43. Hassan, D., S. Janes, and R. Clasen, *Proton-conducting ceramics as electrode/electrolyte materials for SOFC's—part I: preparation, mechanical and thermal properties of sintered bodies.* Journal of the European Ceramic Society, 2003. **23**(2): p. 221-228.
44. El-Meliegy, E. and R. Van Noort, *Glasses and Glass Ceramics for Medical Applications*. 2011: Springer.
45. Scherban, T., et al., *Raman scattering study of phase transitions in undoped and rare earth ion-doped BaCeO3 and SrCeO3.* Journal of Raman Spectroscopy, 1993. **24**(11): p. 805-814.

Appendix

Appendix A

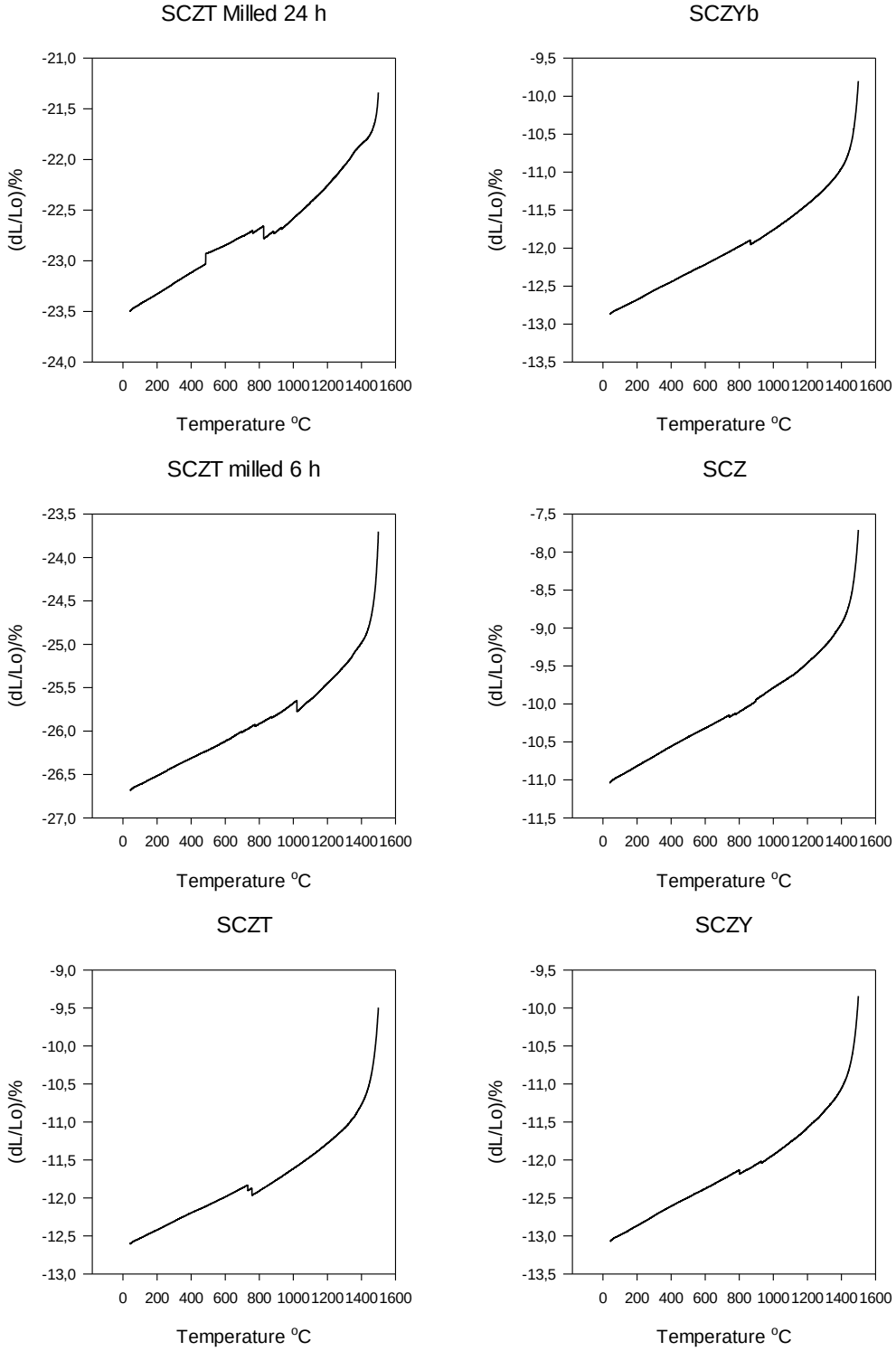

Figure 27 Original cooling curves from dilatometer analysis

Unexpected steps in the curves are likely due to friction between sample and sample holder and have been adjusted for in the calculation of TEC.

Appendix B

Thermal expansion coefficients

TEC \ ˚C	40-200	40-400	40-600	40-800	40-1000	40-1200
SCZT	11,5E-06	11,3E-06	11,0E-06	11,4E-06	12,1E-06	12,8E-06
SCZT 6h	10,8E-06	10,4E-06	10,2E-06	10,1E-06	10,5E-06	11,8E-06
SCZT 24h	10,4E-06	10,5E-06	09,7E-06	09,3E-06	09,7E-06	10,9E-06
SCZYb	11,6E-06	11,7E-06	11,6E-06	11,7E-06	12,1E-06	12,9E-06
SCZY	12,9E-06	12,9E-06	12,4E-06	12,4E-06	12,4E-06	13,4E-06
SCZ	13,6E-06	13,2E-06	12,8E-06	12,3E-06	13,0E-06	13,6E-06

The difference between milled and not milled powder is worth commenting. Alumina contamination from the milling can be reason for a drop in TEC, since polycrystalline Al_2O_3 have a average TEC between 8,6 - 8,8 x 10^{-6}/ ˚C [25], compared to 11,1 x 10^{-6}/ ˚C for SC [9]. The amount of alumina in the powder is probably too small to give such large deviations, but can contribute to the effect.

$SrCeO_3$ do not undergo any phase transitions in the region 77 K - 1000 K, according to Scherban et.al [45], so the secondary phases need to be investigated. Sr_2CeO_4 do have a phase transition in this particular region, and the TEC drops [42]. The amount of residue Sr_2CeO_4 is probably negligible, at least from the XRD results presented in Figure 17. The TEC for Sr_2CeO_4 is also higher than for $SrCeO_3$, so if a significantly part of the membrane consisted of Sr_2CeO_4, higher TEC would be measured.

Synthetic air (YaraPraxair, 5.0) was used as atmosphere during dilatometry. This gas had a CO_2 content of less than 5 vol ppm [39], so reaction between $SrCeO_3$ and CO_2 forming $SrCO_3$ and CeO_2 is possible. Given that 5ppm yields a pCO_2 of 0,55 Pa, the reaction occurs at 5-600 ˚C according to the graph below taken from Kreuer [16]. This matches the temperature region with a decrease in TEC, and could be a possible explanation for the unexpected TEC values.

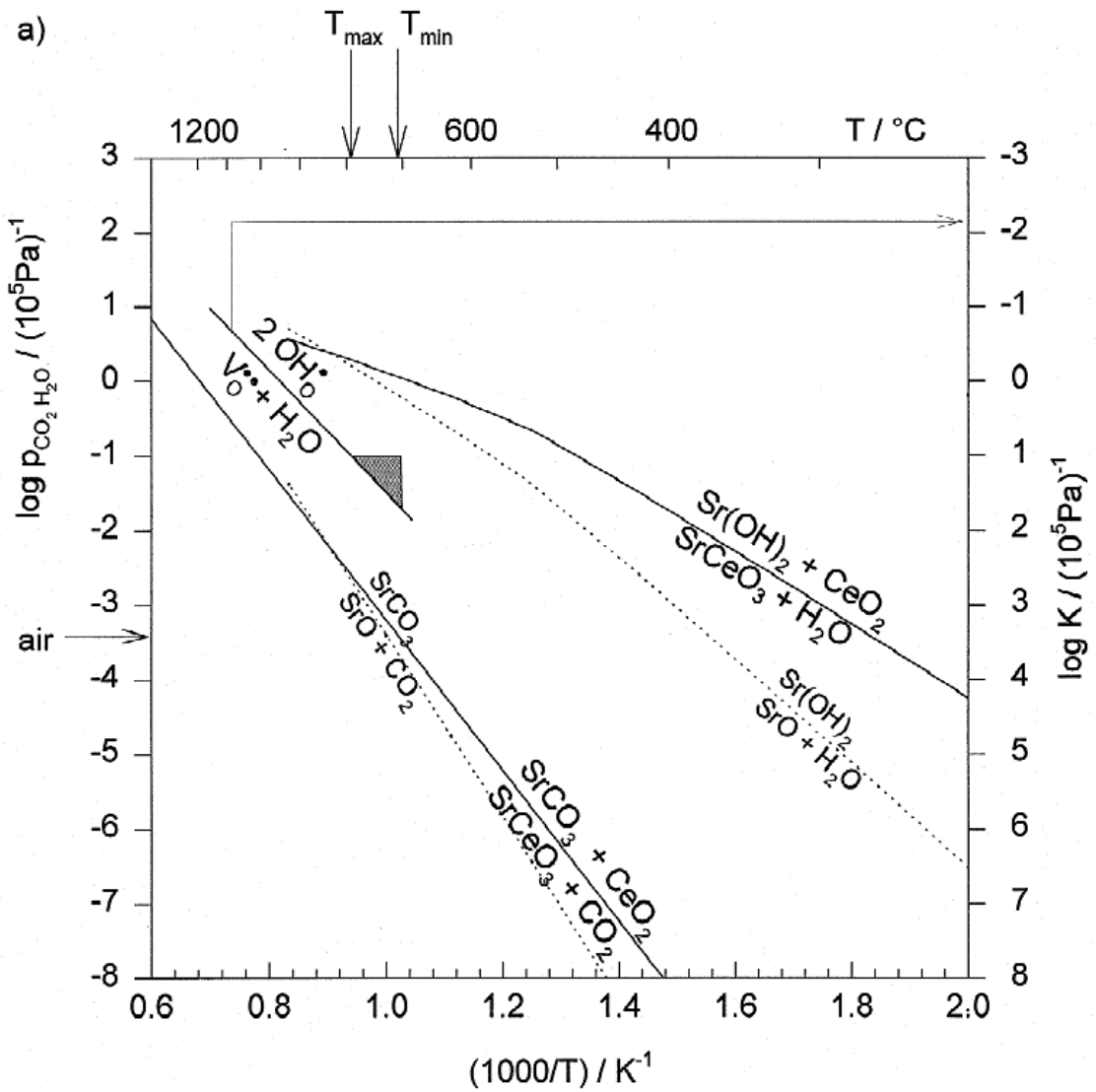

Appendix C

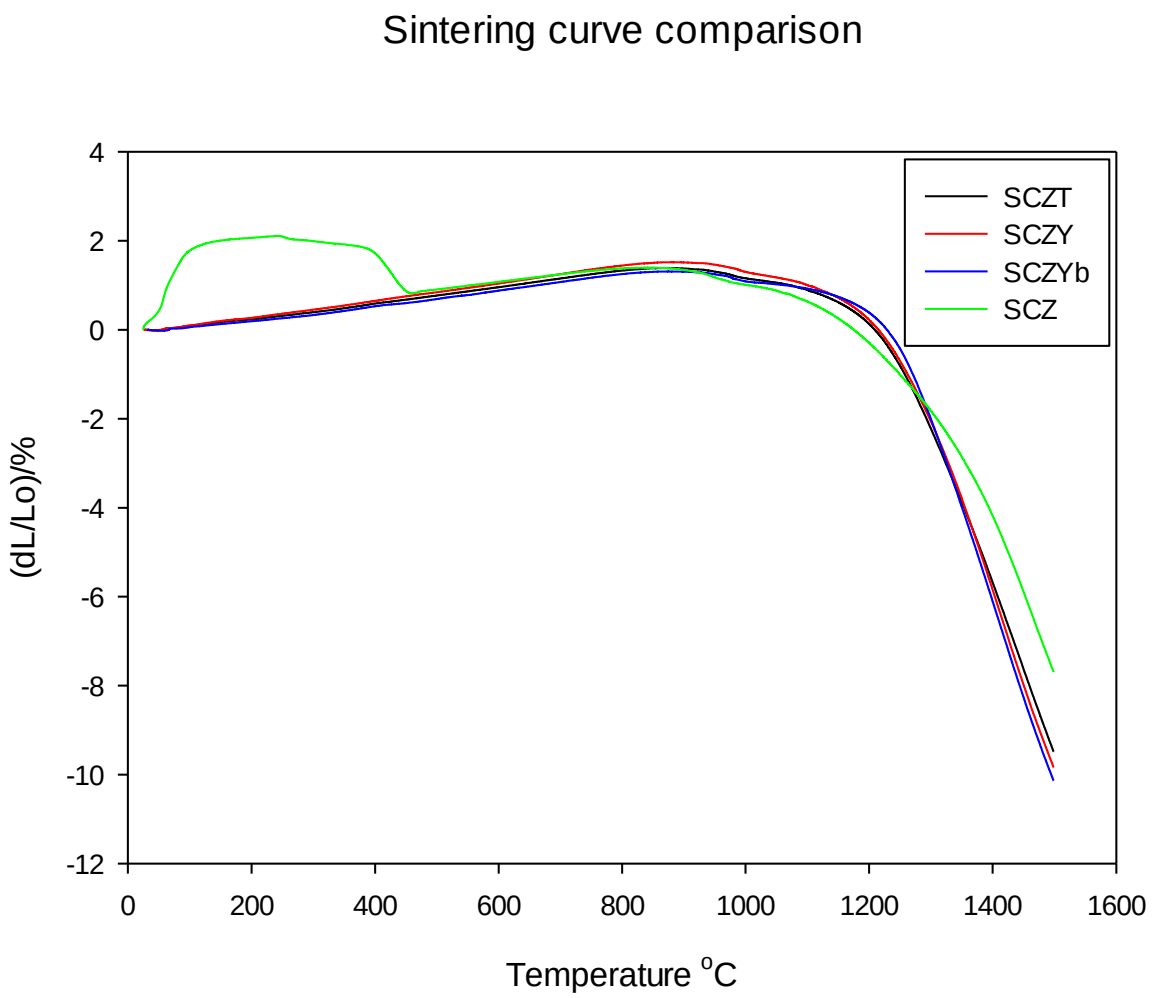

Change in length with respect to initial length plotted against temperature from 40 ˚C - 1500 ˚C. SCZ, represented by the green line in the graph deviate from the other samples. This could be explained by difference in green body density. At 500 ˚C SCZ exhibit the same curve as the other samples, but demonstrates a lower degree of densification than the others. Green body density is known to influence the final density.

Appendix D

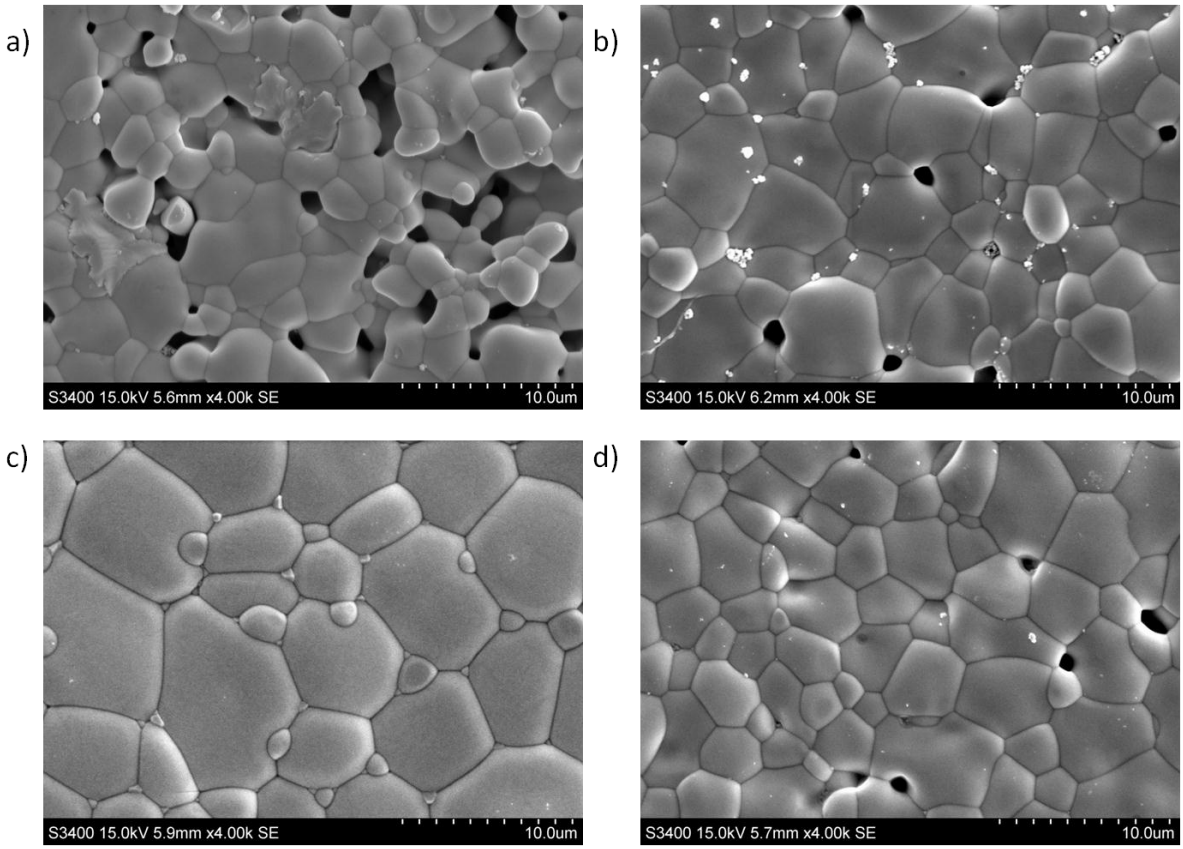

SEM micrographs at 4000X magnification for a) SCZ, b) SCZYb, c) SCZT, d) SCZY. Micrograph of SCZY and SCZYb exhibit pores located on grain boundaries. SCZ have a continuous pore structure and SCZT is completely dense.

Appendix E

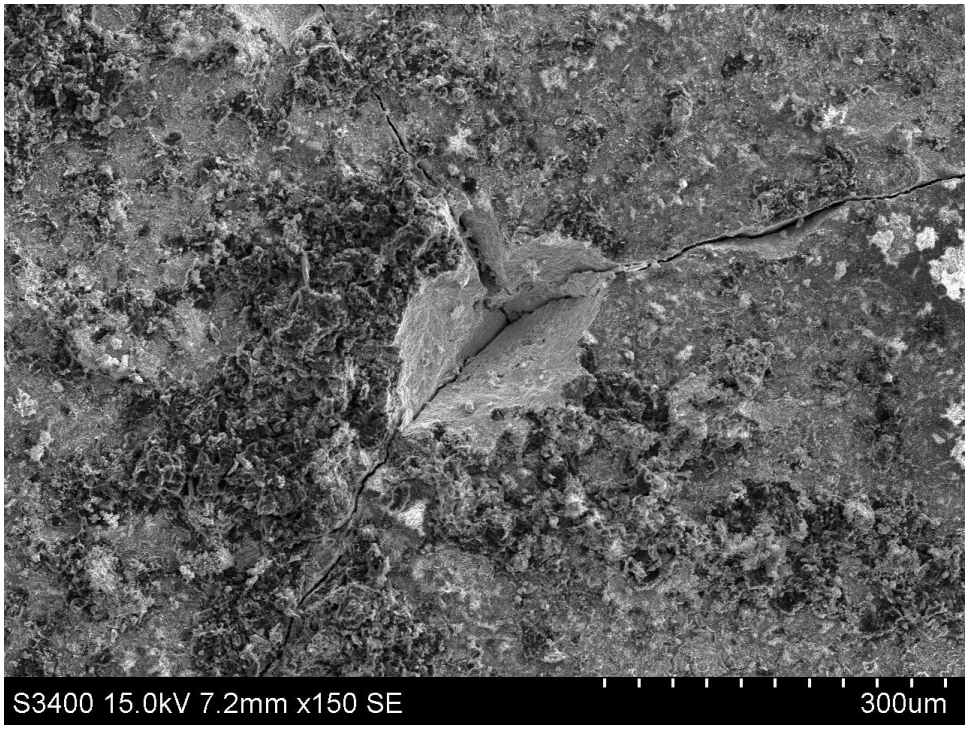

SEM micrograph of not milled SCZT hot pressed at 1400 ˚C with 50 Mpa pressure. The micrograph shows crack formation in the membrane. Due to the extraordinary brittle behavior, handling the sample resulted in further cracking. Grain size measurement proved difficult from the captured micrographs.

Appendix F

										Green Body			
Composition	**Comments**	**crysdens**	**immers.(g)**	**soak(g)**	**Dry(g)**	**T (C)**	**dens (%)**	**Open p(%)**	**Cl.p.(%)**	**D(mm)**	**h(mm)**	**m(g)**	**dens (%)**
SCZT	1500 not milled	5,76	1,2042	1,48	1,3971	17,25	**69,17**	30,06	0,77	15,00	2,91	1,4193	**47,93**
SCZT	1500 milled 6 h	5,76	1,2351	1,4338	1,4348	17,2	**98,61**	-0,50	1,89	10	6,71	1,5023	**49,51**
SCZYb	1500 milled 6 h	5,76	1,257	1,475	1,4743	17,3	**92,30**	0,32	7,38	10	6,48	1,5355	**52,38**
SCZY	1500 milled 6 h	5,66	1,2219	1,4424	1,4411	17,1	**90,78**	0,59	8,63	10	6,31	1,5057	**53,66**
SCZ	1500 milled 6 h	5,71	0,7865	0,955	0,9128	17,2	**74,60**	25,04	0,36	10	4,19	0,9701	**51,63**
SCZT	1600 milled 6h	5,76	1,241	1,4497	1,4487	17,2	**94,79**	0,48	4,73	10	6,92	1,5341	**49,02**
SCZYb	1600 milled 6h	5,76	1,2443	1,4849	1,4841	18	**84,12**	0,33	15,55	10	6,46	1,5221	**52,08**
SCZY	1600 milled 6h	5,66	1,2547	1,4787	1,4774	18,2	**91,49**	0,58	7,93	10	6,57	1,5346	**52,53**
SCZ	1600 milled 6h	5,71	0,8186	0,9687	0,9682	17,6	**88,78**	0,33	10,88	10	4,35	0,9853	**50,51**
SCZT	1600 not milled	5,76	1,2645	1,5114	1,4893	17,6	**82,34**	8,95	8,71	10	6,93	1,5111	**48,22**
SCZYb	1600 not milled	5,76	1,2777	1,5317	1,4877	19	**79,79**	17,32	2,89	10	7	1,5285	**48,26**
SCZY	1600 not milled	5,66	1,1825	1,4323	1,3766	18,6	**76,41**	22,30	1,29	10	6,64	1,4237	**48,22**
SCZ	1600 not milled	5,71	0,6953	0,8584	0,8078	18	**68,14**	31,02	0,84	10	4,67	1,0015	**47,82**
Pre-sintered SCZT Dilatometer		5,76	1,2305	1,4294	1,4277	18	**97,93**	0,85	1,21				